SANDIA REPORT
SAND2022-11794
September 2022

Linear Seismic Source Equivalents in 3D Nonlinear Models: Effects of Embedded Small-Scale, Near-Source Structures

Leiph Preston and Mehdi Eliassi

Prepared by
Sandia National Laboratories
Albuquerque, New Mexico
87185 and Livermore,
California 94550

Issued by Sandia National Laboratories, operated for the United States Department of Energy by National Technology & Engineering Solutions of Sandia, LLC.

Available to DOE and DOE contractors from
U.S. Department of Energy
Office of Scientific and Technical Information
P.O. Box 62
Oak Ridge, TN 37831

Telephone: (865) 576-8401
Facsimile: (865) 576-5728
E-Mail: reports@osti.gov
Online ordering: http://www.osti.gov/scitech

Available to the public from
U.S. Department of Commerce
National Technical Information Service
5301 Shawnee Rd
Alexandria, VA 22312

Telephone: (800) 553-6847
Facsimile: (703) 605-6900
E-Mail: orders@ntis.gov
Online order: https://classic.ntis.gov/help/order-methods/

ABSTRACT

Gaining a proper understanding of how Earth structure and other near-source properties affect estimates of explosion yield is important to the nonproliferation mission. The yields of explosion sources are often based on seismic moment or waveform amplitudes. Quantifying how the seismic waveforms or estimates of the source characteristics derived from those waveforms are influenced by natural or man-made structures within the near-source region, where the wavefield behaves nonlinearly, is required to understand the full range of uncertainty in those yield estimates. We simulate tamped chemical explosions using a nonlinear, shock physics code and couple the ground motions beyond the elastic radius to a linear elastic, full waveform seismic simulation algorithm through 3D media. In order to isolate the effects of simple small-scale 3D structures on the seismic wavefield and linear seismic source estimates, we embed spheres and cylinders close to the fully-tamped source location within an otherwise homogenous half-space. The 3 m diameters spheres, given their small size compared to the predominate wavelengths investigated, not surprisingly are virtually invisible with only negligible perturbations to the far-field waveforms and resultant seismic source time functions. Similarly, the 11 m diameter basalt sphere has a larger, but still relatively minor impact on the wavefield. However, the 11 m diameter air-filled sphere has the largest impact on both waveforms and the estimated seismic moment of any of the investigated cases with a reduction of ~25% compared to the tamped moment. This significant reduction is likely due in large part to the cavity collapsing from the shock instead of being solely due to diffraction effects. Although the cylinders have the same diameters as the 3 m spheres, their length of interaction with the wavefield produces noticeable changes to the seismic waveforms and estimated source terms with reductions in the peak seismic moment on the order of 10%. Both the cylinders and 11 m diameter spheres generate strong shear waves that appear to emanate from body force sources.

ACKNOWLEDGEMENTS

This research was funded by the National Nuclear Security Administration, Defense Nuclear Nonproliferation Research and Development (NNSA DNN R&D). The authors acknowledge important interdisciplinary collaboration with scientists and engineers from LANL, LLNL, MSTS, PNNL, and SNL. This paper describes objective technical results and analysis. Any subjective views or opinions that might be expressed in the paper do not necessarily represent the views of the U.S. Department of Energy or the United States Government.

CONTENTS

LIST OF FIGURES

LIST OF TABLES

ACRONYMS AND TERMS

Acronym/Term	Definition
1D	one dimensional
2D	two dimensional
3D	three dimensional
GF	Green’s function
TVBC	time-varying boundary condition
STF	source time function
MRF	moment rate function
m	meter
s	second
N	Newton
P-wave	primary (compressional) wave
S-wave	shear wave

1. INTRODUCTION

In a prior report (Preston et al., 2021a), we discussed linear equivalent seismic sources of ground motions induced from nonlinear simulations of buried chemical explosions in a 2D cylindrical coordinate system. We have recently expanded this work by evaluating the effects of a variety of nonlinear and near-source parameters used in nonlinear CTH (Schmitt et al., 2017) simulations on the seismic far-field waveforms and on seismic source reconstructions based on those waveforms (Harding et al., in review). However, this most recent work still retains the 2D cylindrical symmetry assumptions used in last year's efforts. Axisymmetric modeling is much less computationally expensive and the parameters evaluated thus far were amenable to this cheaper computation. However, in this report we expand into 3D geometries and evaluate how a few simple 3D shapes affect the seismic wavefield and derive linear seismic source equivalents based on that wavefield.

We evaluate two models with 3 m diameter air-filled cylinders and four models of spheres with diameters of 3 m and 11 m, two air-filled and two filled with basalt. These shapes are embedded in an otherwise homogeneous half space of wet tuff and are offset from the chemical explosive source location so that all simulations use tamped sources. Because air-filled tunnels are common in underground facilities such as mines, the cylinders are meant to approximate these structures. The spheres are meant to evaluate the effects of small-scale structure in the near-field on far-field seismic waves. Two of the spheres have the same diameters as the cylinders, which are much less than the seismic wavelength, and, thus, according to seismic diffraction theory (e.g., Lay and Wallace, 1995) the smallest spheres would be expected to have a negligible effect on the wavefield. However, the larger spheres may be large enough to have a perceptible effect on the wavefield. We desired to assess to what extent these small-scale structures situated clearly within the nonlinear portion of the wavefield affect seismic moments estimated from the far-field waveforms.

The details of the models and methods used, including CTH parameters used in the nonlinear simulations, linear seismic modeling, and the linear source time function inversion will be provided in Section 2. The results of the source time function inversions will be reported and discussed in Section 3. Finally, in Section 4 we will conclude with a brief summary of results and future directions.

2. MODELS AND METHODS

In this section we describe the Earth models used in both the nonlinear and linear simulations and the parameters used in both algorithms. We will also discuss the methods used to go from CTH output to source time functions (STFs), which comprise the linear seismic source equivalents.

2.1. CTH (Nonlinear) Models and Parameters

We used CTH, Sandia's shock physics code (Schmitt et al., 2017), to simulate three-dimensional (3D) tamped explosions of 18 metric tons of Comp-B, at a depth of burial of 250 m (more specifically, we located the center of the spherical explosive charge at x=0, y=0, and z=-250 m). As Table 2.1 lists, we simulated seven different cases, where, except for the fully tamped case (i.e., Case# 5 or BL designation in the report), the other six cases included some kind of inclusion. The inclusions consisted of cylindrical air-filled tunnels (Case# 1 and 2), spherical air-filled cavities (Case # 3 and 6), and a spherical basalt inclusion (Case# 4 and 7). Table 2.1 also provides the physical description of each inclusion, although it is worth noting here that all cases with inclusions have the inclusion center at x=12, y=0, z=-250 m.

We performed all simulations on Sandia's Attaway High Performance Computing Capacity Cluster Platforms, using 800 nodes (i.e., 28,800 cores). Table 2.1 lists the CPU hours for each case, where the fully tamped cases (BL) had the lowest CPU hours and all other cases that we included inclusions required more CPU-hours.

Table 2.1. Description of simulated 3D CTH cases

Case #	Ground Material	Inclusion Shape/Dimensions	CPU (Hrs.)	Designation in Report
1	Wet tuff	Air filled cylindrical tunnel, centered at x=12, y=0, z=-250 m, radius=1.5 m, extended from -1.28 km≤y≤1.28 km	10.3	infTun
2	Wet tuff	Air filled cylindrical tunnel, centered at x=12, y=0, z=-250 m, radius=1.5 m, extended from -1.28 km≤y≤0.0015 km	13.8	halfTun
3	Wet tuff	Air-filled spherical cavity, centered at x=12, y=0, z=-250 m with radius=1.5 m	6.3	airSph3
4	Wet tuff	Basalt-filled spherical solid, centered at x=12, y=0, z=-250 m with radius=1.5 m	12.4	basSph3
5	Wet tuff	Fully tamped, No inclusion	5.9	BL
6	Wet tuff	Air-filled spherical cavity, centered at x=12, y=0, z=-250 m with radius=5.5 m	7.5	airSph11
7	Wet tuff	Basalt-filled spherical solid, centered at x=12, y=0, z=-250 m with radius=5.5 m	16.6	basSph11

2.1.1. Nonlinear Domain Earth Models

For all nonlinear CTH simulations, the computational domain for the x- and y-directions respectively ranged as -1,280 m≤x≤1,280 m and -1,280 m≤y≤1,280 m. The computational domain depth (i.e., z-direction) for all cases was 2,560 m thick. The first three cases ranged from -2,460 m≤z≤100 m, where z=0-100 m was the atmosphere above the ground and z<0 included the ground materials. Our preliminary seismic signal analyses showed high-frequency noise near the air-ground region, which we attributed to the layer of atmosphere not being thick enough. For the subsequent four cases, we increased the thickness of atmosphere to 400 m and the resulting ground material thickness was 2,160 m. The high-frequency noise in the first three cases, however, did not impact results as post-process filtering removed this noise. We note that the maximum grid resolution for each simulation was 100 cm, using CTH Adaptive Mesh Refinement approach. Although this is not sufficient to finely resolve the geometry of the charge and inclusions, CTH ensures that all masses inserted into the model are correct and conserved during the simulation. Given the rather low frequencies used in our analysis (see Section 2.2.2) these geometric differences are expected to have a negligible impact on results.

2.1.2. *CTH Algorithmic Parameters*

The key models (and their parameters) for our CTH simulations include the choice of Equation-of-Sate (EOS) for each material (i.e., air or ground), the explosive burn model, and material strength/fracture model. In this work, the wet tuff EOS was SESLAN/7120 with an initial density of 1.95 g/cm^3. We used ideal gas EOS for air. For cases where we included basalt inclusions, the basalt EOS was SESLAN/7530 with an initial density of 2.87 g/cm^3. We used the Jones-Wilkins-Lee (JWL) EOS burn model to detonate the explosive charge (from the center of the charge). We used a linearized version of Johnson-Cook (JC) flow stress and damage model as the material strength model for the wet tuff. For Case# 4 and 7, we used the Geological-Yield Surface (GEO) strength model to simulate the basalt strength. In Eliassi and Preston (2022), we provide detailed explanations for JWL burn, JC, and GEO strength models and refer interested readers to that work. Moreover, in that work we also list the JWL EOS parameter values, which we also used for all simulations in the current report.

Below, we list the JC flow stress model parameters for the wet tuff. Again, Eliassi and Preston (2022) provide additional explanation for each parameter listed here.

Table 2.2. JC flow stress parameters for wet tuff

Material	AJO (kb)	BJO (kb)	NJO (-)	CJO (-)	MJO (-)	Melt Temp (K/eV)	Poisson's Ratio	P_{frac} (kb)
Wet tuff	0.05	0.0	0.0	0.0	1	1973/0.17	0.25	-0.05

The JC damage model parameters for wet tuff consisted of D1=D2=1/2, D3=-10, D4=D5=0. The list of GEO material strength model parameters for the basalt cases are listed in Table 2.3. These parameters are the same we report in Harding et al. (in review).

Table 2.3. GEO material strength model parameters for basalt

Material	Y_0(kb)	Y_∞ (kb)	$\frac{dY}{dP}$ (DYDP)	Melt Temp (K/eV)	Poisson's Ratio	P_{frac} (kb)
Basalt	0.001	0.9	2	1973/0.17	0.3	-0.025

2.1.3. *Representative CTH Results*

While the focus of this report is not the nonlinear (i.e., CTH) results directly, it might be useful to show representative results for the 3D simulations. Figure 2.1 compares the velocity magnitude plots for the fully tamped (BL), 3 m diameter air sphere (airSph), and 3 m diameter basalt sphere

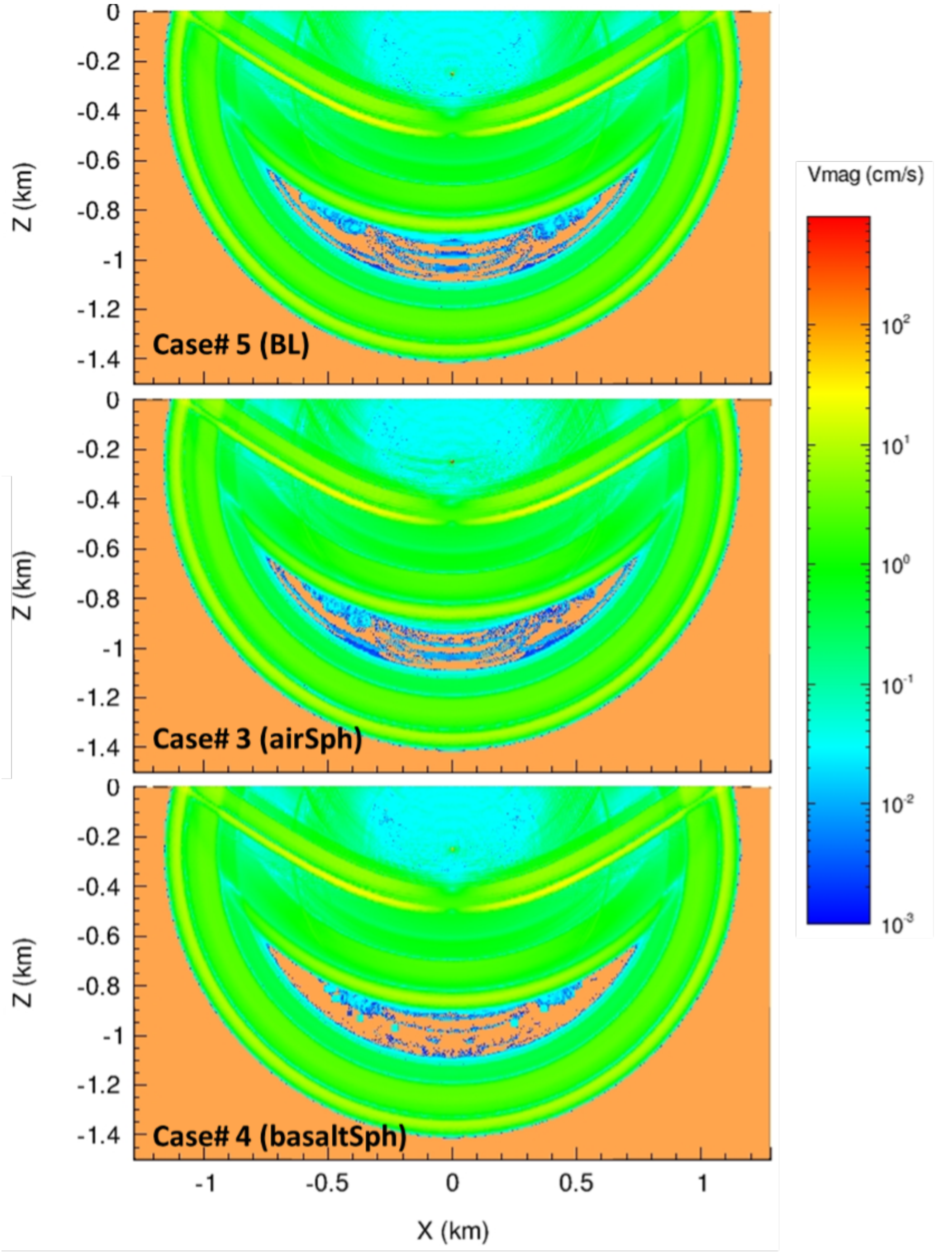

Figure 2.1. XZ plane cross-section (y=0 m) views of the CTH velocity magnitude for three cases after 0.35 s, comparing the fully tamped, 3 m diameter air sphere, and 3 m diameter basalt inclusions. The insets for each image state the case and the top of the color bar is set at 800 cm/s. The background (Peru color) represents the wet tuff. Note that the spherical inclusions are not visible at this scale.

(basaltSph) after 0.35 s. We chose this plot time as the shock front has not reached the side boundaries (i.e., extents of X and Y domains). Clearly, the shock expansion is similar in all three cases. Figure 2.2 is a similar comparisons, except we are comparing the 11 m diameter air sphere and the 11 m diameter basalt sphere with the baseline fully tamped case. In these cases we also observe relatively similar extent of the ground shock response to the previous figure. However, we do see small differences inside the shock between the 3 m and 11 m diameter air sphere. Yet, the interesting point is regardless of the type of inclusion, the nonlinear ground response is quite similar to that of

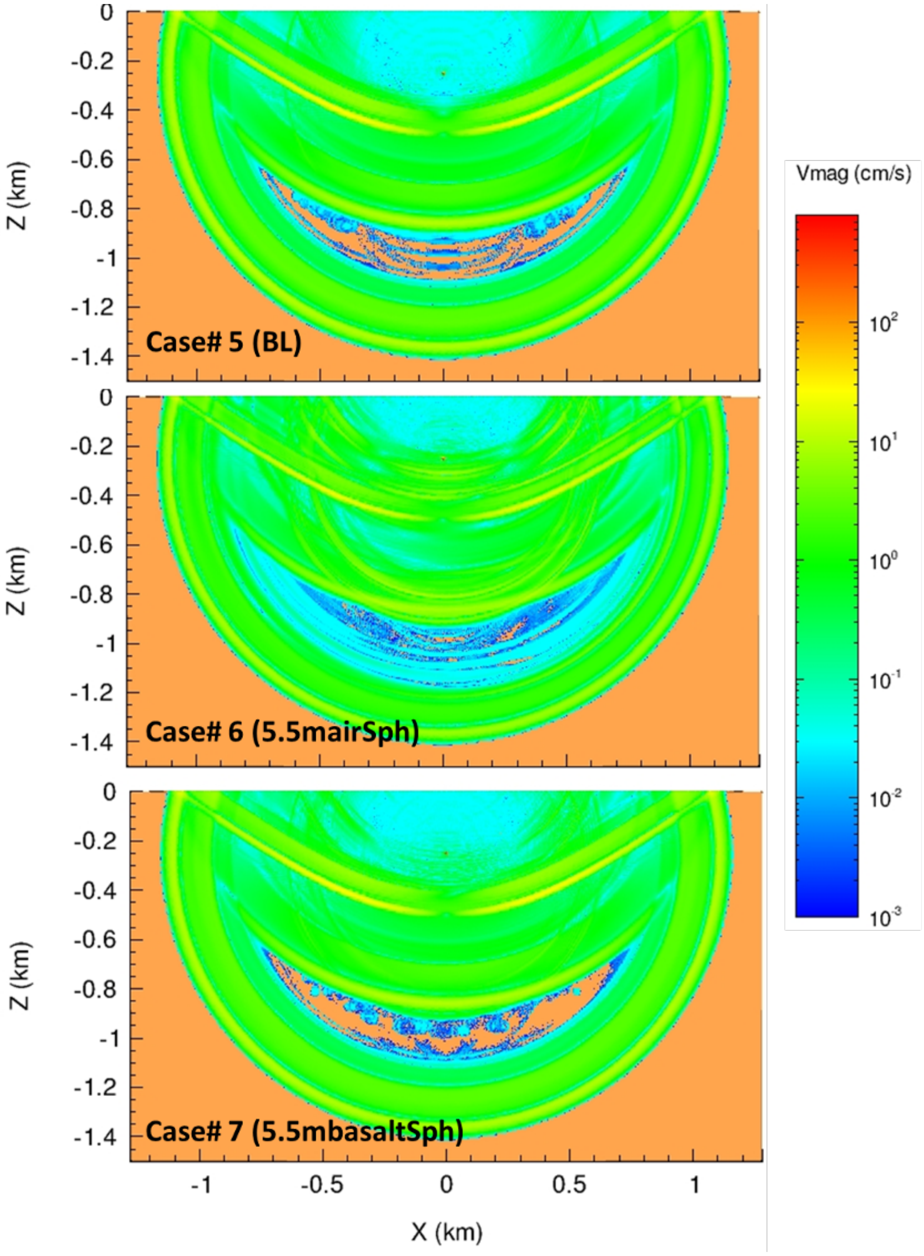

Figure 2.2. XZ plane cross-section (Y=0 m) views of the CTH velocity magnitude for three cases after 0.35 s, comparing the fully tamped, 11 m diameter air sphere, and 11 m diameter basalt inclusions. The insets for each image state the case and the top of the color bar is set at 800 cm/s. The background (Peru color) represents the wet tuff. Note that the spherical inclusions are not visible at this scale.

a fully tamped case. It is important to keep in mind we might not be fully resolving the various inclusions and we might need a finer mesh (i.e., a lot more computational resources) to properly resolve such complex effects as tunnels and potentially other heterogeneities.

2.2. Parelasti (Linear) Models and Parameters

2.2.1. Linear Domain Earth Model

For the linear domain modeling we used only one Earth model independent of the model used in the nonlinear domain. This model was a homogeneous half-space consisting of wet tuff (Table 2.4) and an explicit stress-free surface condition to approximate the air-earth interface.

Table 2.4. Linear domain earth model parameters

Material	Vp (m/s)	Vs (m/s)	Density (kg/m^3)
Wet tuff	3278	1892	1950

2.2.2. Parelasti Parameters

The linear 3D seismic simulations are computed by the code Parelasti (e.g., Poppeliers and Preston, 2020). Parelasti solves the linearized velocity-stress systems of partial differential equations on a standard staggered grid with second order accurate finite-difference operators in time and fourth order accurate operators in space. We use Parelasti in two different ways to produce simulated wavefields, using: 1) time-varying boundary conditions (TVBCs) and 2) point impulse sources to produce Green's functions (GFs).

As discussed above, CTH is used to compute the wavefield while it is in the shock regime and nonlinear effects are significant. However, as the wavefield propagates farther from the source, nonlinear effects wane and the wavefield eventually reaches a distance, termed the elastic radius, beyond which it can be well-approximated using linear seismic theory. Thus, Parelasti, which is much less computationally expensive than a nonlinear algorithm (e.g., Preston et al., 2021a), can be used to propagate the wavefield once it is beyond the elastic radius. To accomplish this, tracer output of 3D particle velocities and stresses from CTH is used as TVBCs within Parelasti (Preston et al., 2021b). The tracers, and thus the TVBCs, form a cylinder with a radius 170 m horizontally and end caps 170 m above and below the source (Figure 2.3). Multiple TVBC distances were evaluated and it was determined that 170 m was at a sufficient distance from the source to be beyond the elastic radius for the medium and source's emplacement conditions (Preston, 2017). Since velocities and stresses must be known at every point on the TVBC surface, the grid node spacing in Parelasti is the same as the tracer spacing, which is 5 m. CTH tracer data is resampled to match the Parelasti time step and filtered with a second-order Butterworth filter with a 17 Hz lowpass cutoff frequency, ensuring that minimal numerical dispersion will be present in the Parelasti simulations (e.g., Aldridge and Haney, 2008).

The TVBCs drive the 3D wavefield, which is propagated by Parelasti to a set of 73 receivers that surround the source detonation point in a cube at 500 m on all sides but directly above the source (Figure 2.3). This arrangement is solely meant to allow the source radiation pattern to be well sampled and is not meant to represent a realistic geometry of receivers. These three component receivers record the particle velocities that form our "observed" data, thus called because they are derived from the CTH nonlinear simulations.

The other way in which Parelasti is used is to produce linear seismic GFs. In this mode, a point source with an impulse source time function is directly inserted into Parelasti at the source detonation point (i.e., x=0, y=0, z=-250 m). In this work we utilize two basic source types: an isotropic moment tensor and body forces. An isotropic moment tensor is a far-field approximation

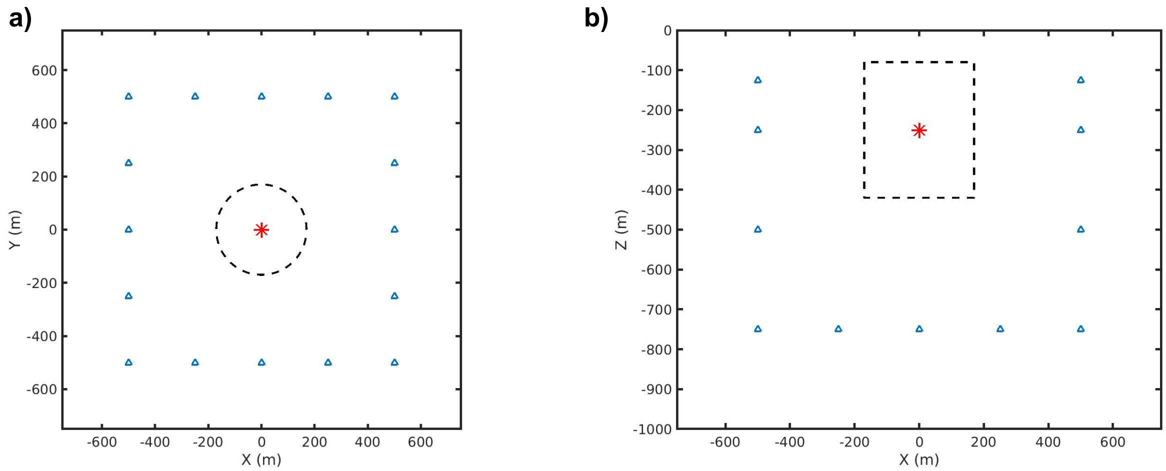

Figure 2.3. a) XY plane cross-section and b) XZ plane cross-section of TVBCs (dashed black) and receivers (blue triangles) in Parelasti. Source location is indicated by the red asterisk. The TVBCs form a cylinder with vertically oriented symmetry axis. Receivers form a cube around the source location except directly over the source.

of an explosion source and is represented by three mutually orthogonal force couples acting on the source point. A body force is simply a force applied in a single direction at the source point. Parelasti is used to propagate the wavefield produced by this point source to the same set of receivers as used for the TVBCs above (Figure 2.3). It is important to note that the GFs use Parelasti throughout and no information from the nonlinear calculations is used to produce them. Also, since all the linear simulations use the same homogeneous half-space Earth model, all GFs assume a fully tamped source without any 3D structure within the Parelasti domain; thus, the GFs are ignorant of the true 3D structure used in the CTH simulations.

2.3. Source Time Function Inversion

Once we have the "observed" data and GFs at the same set of receiver points, we are able to invert the observed data for the STFs. These STFs describe which linear point source types are able to optimally fit the data and how the strength of those sources vary with time. The STFs thus describe the optimal linear equivalent sources for the actual nonlinear processes that occur in the near-source region. The linear equivalent sources are the sources that are implied by using linear seismic theory on far-field seismic data, assuming point sources and simple combinations of forces or force couples acting at the source point.

In linear seismic source theory, the observed data is the sum of the convolutions of GFs with their respective STFs (e.g., Aki and Richards, 2002):

$$O_j(t) = \sum_{i=1}^{N_S} G_{ij}(t) * S_i(t)$$

where $O_j(t)$ is the observed data for channel j of the receiver network (i.e., a seismogram), N_S is the number of different source types, $G_{ij}(t)$ is the GF from the i^{th} source observed on the j^{th} channel, $S_i(t)$ is the i^{th} STF, and * represents time-domain convolution.

In the time domain, discrete convolution can be represented as the product of a matrix in Toeplitz form with a vector. The Toeplitz matrix is formed by using the GF as its first column and shifting the GF by one sample for each subsequent column for N_T columns, where N_T is the number of time samples. All elements not occupied by GF elements are set to zero. This forms a matrix with $2N_T - 1$ rows. For an STF with N_T samples, the matrix-vector product hence produces a $2N_T - 1$ by 1 vector as expected for discrete convolution. However, the observed data are only N_T samples long. Although there are other options, we choose to truncate the matrix-vector product at N_T samples. This is equivalent to truncating the Toeplitz matrix at N_T rows, which, of course, then makes the Toeplitz matrix a lower diagonal square matrix. Hence, for one STF and one observed seismogram

$$\begin{bmatrix} d_1 \\ d_2 \\ \vdots \\ d_{N_T} \end{bmatrix} = \begin{bmatrix} G_1 & 0 & \cdots & 0 \\ G_2 & G_1 & 0 & \vdots \\ \vdots & \vdots & \ddots & 0 \\ G_{N_T} & G_{N_T-1} & \cdots & G_1 \end{bmatrix} \begin{bmatrix} s_1 \\ s_2 \\ \vdots \\ s_{N_T} \end{bmatrix} \Delta t$$

where subscripts indicate time samples and Δt is the time sample interval (due to discrete integration in the convolution), d is the vector of observed data, G_i is the i^{th} time sample of the GF, and s is the STF vector. This can be condensed into the form

$$d = \mathbf{G} s \Delta t \tag{2.1}$$

If there are N_R receiver channels and N_S sources then the system can be expanded by appending rows and columns such as

$$\begin{bmatrix} d_1 \\ d_2 \\ \vdots \\ d_{N_R} \end{bmatrix} = \begin{bmatrix} \mathbf{G_{1,1}} & \mathbf{G_{1,2}} & \cdots & \mathbf{G_{1,N_S}} \\ \mathbf{G_{2,1}} & \mathbf{G_{2,2}} & \cdots & \mathbf{G_{2,N_S}} \\ \vdots & \vdots & \ddots & \vdots \\ \mathbf{G_{N_R,1}} & \mathbf{G_{N_R,2}} & \cdots & \mathbf{G_{N_R,N_S}} \end{bmatrix} \begin{bmatrix} s_1 \\ s_2 \\ \vdots \\ s_{N_S} \end{bmatrix} \Delta t \tag{2.2}$$

where here each d_i is an entire observed seismogram for receiver-channel i of length N_T, each $\mathbf{G_{i,j}}$ is a full square Toeplitz matrix as described above for source j recorded on receiver-channel i, and each s_j is the STF for source j. Thus, for the entire system above, the left-hand side has a size $N_R N_T$ by 1, the matrix has a size $N_R N_T$ by $N_S N_T$, and the right-hand vector of STFs has a size $N_S N_T$ by 1.

Although Equation 2.1 is mathematically proper, we find in practice that we can obtain more stable and faster convergence in solutions if we solve for moment rate functions (MRFs), or the time derivative of the STFs, instead of the STFs directly. We believe this is due to the fact that far-field waveforms have only weak dependence on the lowest frequencies of the STF since the far-field wavefield is dominated by the second-time derivative of moment STFs and first derivative of force STFs (e.g., Aki and Richards, 2002; Aldridge, 2000). Equation 2.1 can be cast to use MRFs via

$$\dot{d} = \mathbf{G} \dot{s} \Delta t \tag{2.3}$$

where $\dot{d}$ is the time derivative of the observed data and $\dot{s}$ is the MRF. In this study, the observed seismogram is in units of velocity; thus, the left-hand side of Equation 2.3 is in units of acceleration.

One of the major reasons for performing the STF inversion in the time domain is that we can more precisely control regularization, which is generally required for numerical stability of the inversion. We add two forms of regularization to the system in Equation 2.3. To damp high frequency noise in the solutions, we impose smoothing regularization in the form of a 1D Laplacian operator. In matrix form the Laplacian regularization has the form

$$L_S = \begin{bmatrix} 1 & -2 & 1 & 0 & \cdots & 0 \\ 0 & 1 & -2 & 1 & 0 & \vdots \\ \vdots & 0 & \ddots & \ddots & \ddots & 0 \\ 0 & \cdots & 0 & 1 & -2 & 1 \end{bmatrix} \frac{1}{\Delta t^2}$$

Secondly, we expect the MRFs to asymptote toward zero at later times, so we apply a minimum solution norm constraint as well, but only apply this constraint to later portions of the solution. The full matrix that implements this regularization is

$$L_Z = \begin{bmatrix} 0 & 0 & & \cdots & & 0 \\ 0 & \ddots & \ddots & & & \\ & \ddots & 0 & 0 & & \vdots \\ \vdots & & 0 & 1 & 0 & \\ & & & 0 & \ddots & 0 \\ 0 & & \cdots & & 0 & 1 \end{bmatrix}$$

Note that the typical identity matrix form of minimum norm solution does not start until farther down on the diagonal. The time sample where this starts is determined by the user. Obviously, the empty rows above the start time of the regularization can be removed but are shown above to make its connection to traditional minimum solution norm implementations.

Finally, we can weight the data so that certain portions of the observed data are fit better than others. We expect that the clearest and least contaminated portion of the waveform to be the initial arrivals of either P or S, depending on the channel. Due to imperfections in Earth models, the later arrivals will have more opportunity to be influenced or interfered with from arrivals due to Earth structure that is not represented in the GFs, whereas initial arrivals can be more easily aligned to compensate for arrival time errors. Because of this, we desire to give higher weight to the initial arrival window for P and/or S. To achieve this, we give unit weighting to the observed data and GFs up to a time equal to that computed from a move-out velocity (v) plus a time window length (t_w) meant to capture the first arriving wave pulse. After this time, the weight is decreased according to a gaussian with a standard deviation (σ) specified by the user. For a receiver at distance r from the source, the weighting function is thus

$$w(t) = \begin{cases} 1 & t \le t_o \\ \exp\left(-\frac{(t - t_o)^2}{2\sigma^2}\right) & t > t_o \end{cases}$$

with $t_o = \frac{v}{r} + t_w$.

An S-wave window can also independently be applied. If so, the above-described P-wave weighting window is used until the computed time from the S-velocity move-out, at which point the weight jumps back up to unity and remains such until the end of the S time window, before decreasing again according to a half gaussian.

The entire system can now be constructed using the data and regularization matrices as

$$\begin{bmatrix} w\dot{d} \\ \mathbf{0} \\ \mathbf{0} \end{bmatrix} = \begin{bmatrix} w\mathbf{G} \\ \alpha\mathbf{L_S} \\ \beta\mathbf{L_Z} \end{bmatrix} \dot{s}\Delta t \qquad (2.4)$$

where w is the time-weighting functions as described above, and α and β are regularization parameters (scalars) that are used to control the strength of each of the regularization terms relative to the fit to the observed data. We solve the linear system of equations in Equation 2.4 using conjugate gradient least squares (Hestenes and Stiefel, 1952) for the MRFs, $\dot{s}$.

The above system of equations forms a large, dense system of equations that can be extremely computationally expensive to solve. That is why in our prior work (e.g., Poppeliers and Preston, 2020; Preston et al., 2021a) we solved for the STFs in the frequency domain, where the equations are much more computationally tractable. However, as noted above, solving for the STFs in the frequency domain makes it difficult to apply the regularizations and data weightings that we describe above, which allows us to precisely control how well different portions of the wavefield are fit or regularized versus other portions. In order to make the system in Equation 2.4 more computationally tractable, we downsample the observed data and GFs, after applying appropriate anti-alias filters, by a factor of 8. Thus, the resultant MRFs are likewise downsampled. The first step of post-processing is to numerically integrate the MRFs to form STFs and to upsample to the original time sample rate.

3. RESULTS

Example traces and the resultant STFs for each of the evaluated geometries are shown and discussed in this section. A baseline case is used as a reference for comparison with results. The

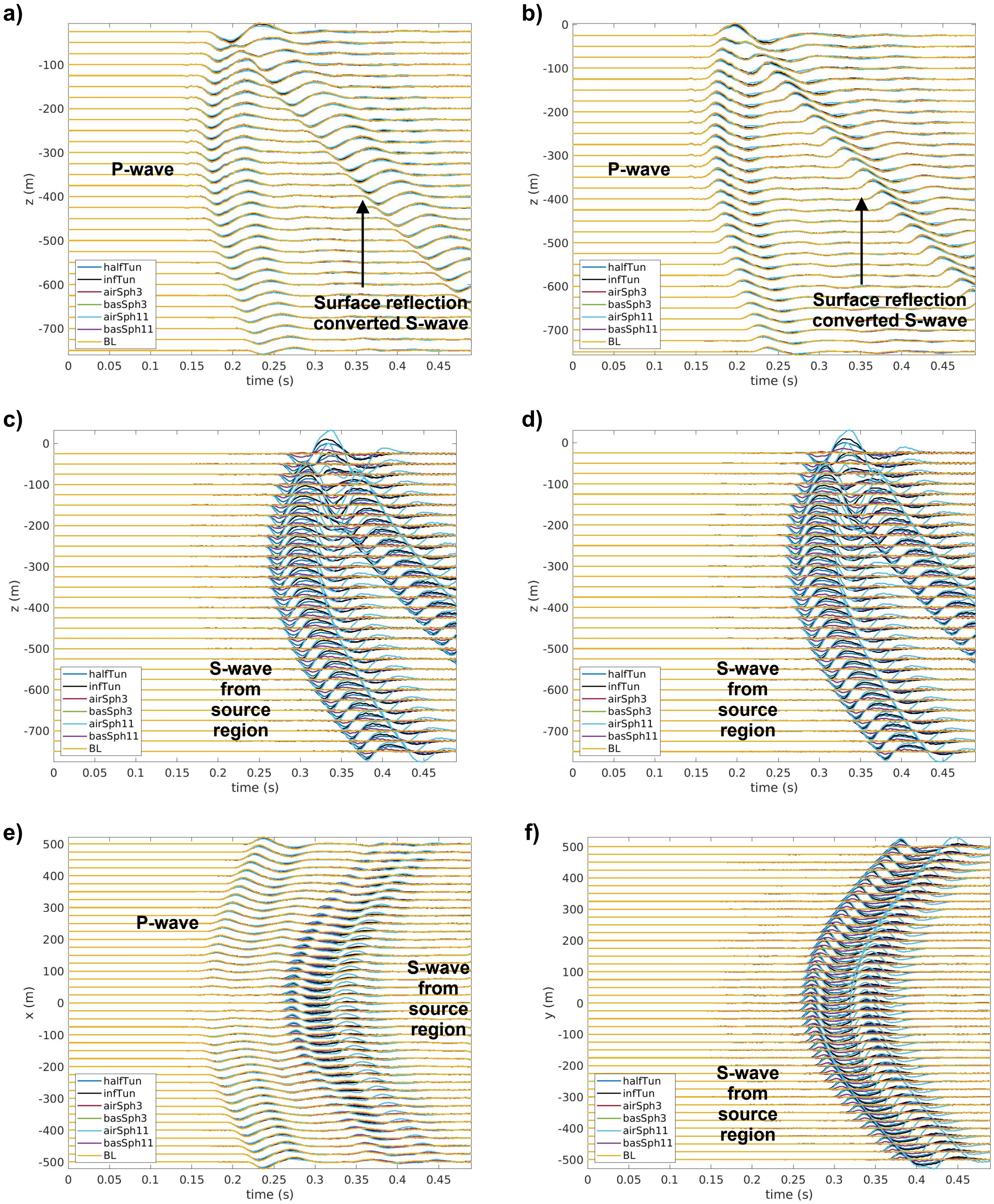

Figure 3.1: Comparison of Vx waveforms: infinite tunnel, half tunnel, air-filled sphere, basalt-filled sphere, and baseline (BL). At y=0 m and a) at x=+500 m, b) x=-500 m, c) y=+500 m, d) y=-500 m, e) z=-750 m; f) at x=0 m and z=-750 m. Principle seismic arrivals are labeled. See Figures A.1-A.6 for more detailed images.

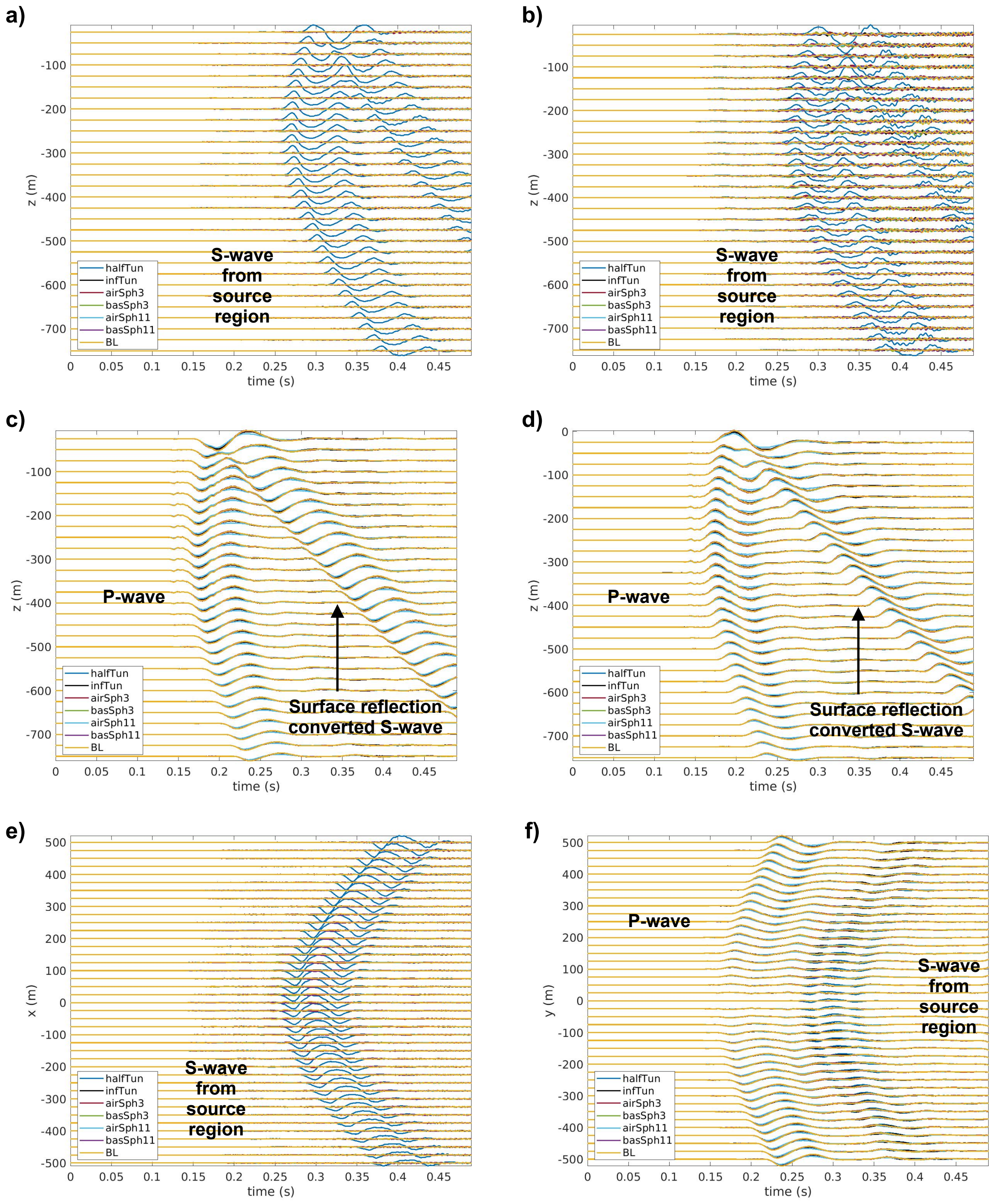

Figure 3.2: Comparison of Vy waveforms: infinite tunnel, half tunnel, air-filled sphere, basalt-filled sphere, and baseline (BL). At y=0 m and a) at x=+500 m, b) x=-500 m, c) y=+500 m, d) y=-500 m, e) z=-750 m; f) at x=0 m and z=-750 m. Principle seismic arrivals are labeled. See Figures A.7-A.12 for more detailed images.

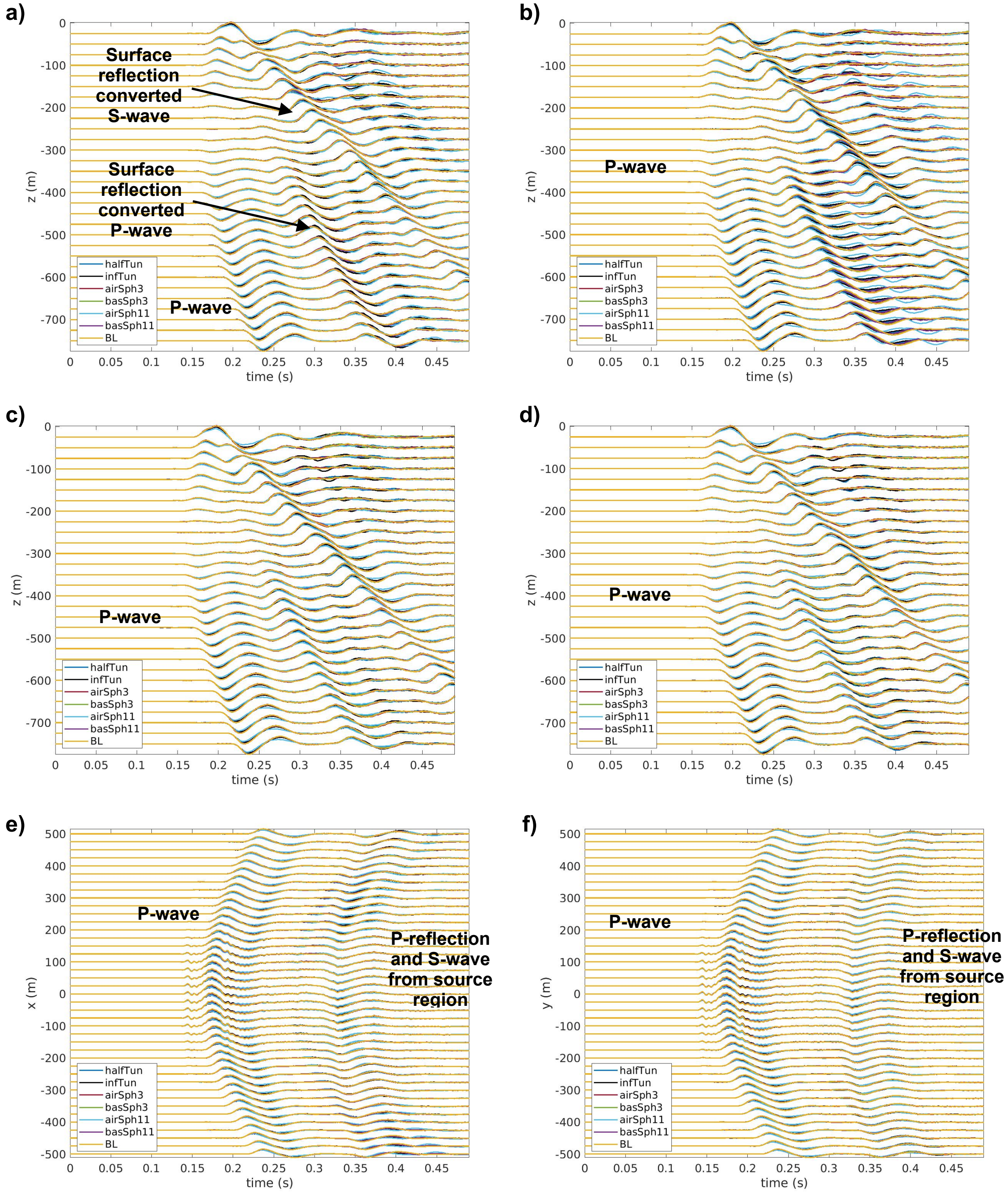

Figure 3.3: Comparison of Vz waveforms: infinite tunnel, half tunnel, air-filled sphere, basalt-filled sphere, and baseline (BL). At y=0 m and a) at x=+500 m, b) x=-500 m, c) y=+500 m, d) y=-500 m, e) z=-750 m; f) at x=0 m and z=-750 m. Principle seismic arrivals are labeled. See panel a) labels for similar arrivals on b). See Figures A.13-A.18 for more detailed images.

baseline case is a 3D tamped simulation without any 3D structure in the CTH model, i.e., a homogeneous half space. Processing with Parelasti and inversion for the STFs is the same as all other cases.

3.1. Infinite Cylinder

As described in Section 2, the infinite cylinder case consists of a 3 m diameter air-filled cylinder with its center 12 m offset in the x-direction from the source point that runs “infinitely” in the plus and minus y direction. This represents a long tunnel near a detonation point that has been well-stemmed to contain the explosion. Strong shear waves are generated that are particularly visible on the Vx component at y=+/- 500 m and at z=-750 m (Figure 3.1c,d,e; A.3-A.5), which are not expected in a homogeneous half space. Figure 3.1-3.3 (Figures in Appendix A provide more detailed images) also shows smaller but still visible differences on other channels, which look like perturbations on top of the baseline waveforms, such as Vz at x=+/- 500 m (Figure 3.3a,b; A.13, A.14). These latter differences appear to generally reduce the amplitude of the initial P wave and scatter that energy into later portions of the wavefield. Some of the biggest differences, besides the aforementioned shear waves, are in the surface reflection-converted shear waves and the incipient surface wave on their tail end as seen on receivers shallower than the source depth. Also, forward-scattered energy (Figures 3.1-3.3a; A.1, A.7, A.13) shows less perturbation to the wavefield than back-scattered energy (Figures 3.1-3.3b; A.2, A.8, A.14). It should be noted that, in general, the infinite cylinder showed larger differences from the baseline waveforms compared to the half tunnel case, which is not unexpected, but generally smaller differences from baseline compared to the 11 m diameter air-filled sphere.

This is borne out by the explosion STFs computed for the infinite cylinder (Figure 3.4a). The reduction in the directly arriving P mentioned above has a clear impact on the STF with a peak seismic moment ~13% smaller than the baseline STF. The strong shear waves on the Vx component visible on receivers offset from the source in the y and z directions show nearly isotropic shear generation in those directions. This shear wave radiation pattern suggests a horizontal body force source pointed in the x-direction, Fx (e.g., Aldridge, 2000). The resulting STF for the Fx portion of the source is shown in Figure 3.4b and how well the combined explosion + Fz source fits

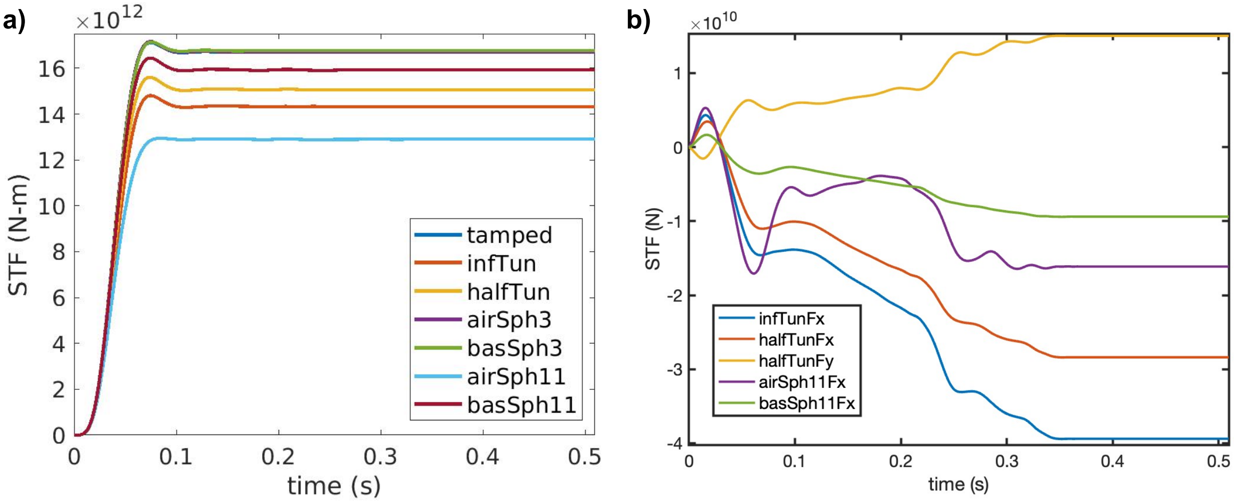

Figure 3.4: a) Comparison of explosion portion of the STFs for the tamped (baseline) case, infinite tunnel, half tunnel, 3 m air-filled sphere, 3 m basalt sphere, 11 m air-filled sphere, and 11 m basalt sphere. b) Comparison of force source portions in the infinite tunnel and half tunnel cases. The explosion STFs for the tamped and both 3 m spheres significantly overlap.

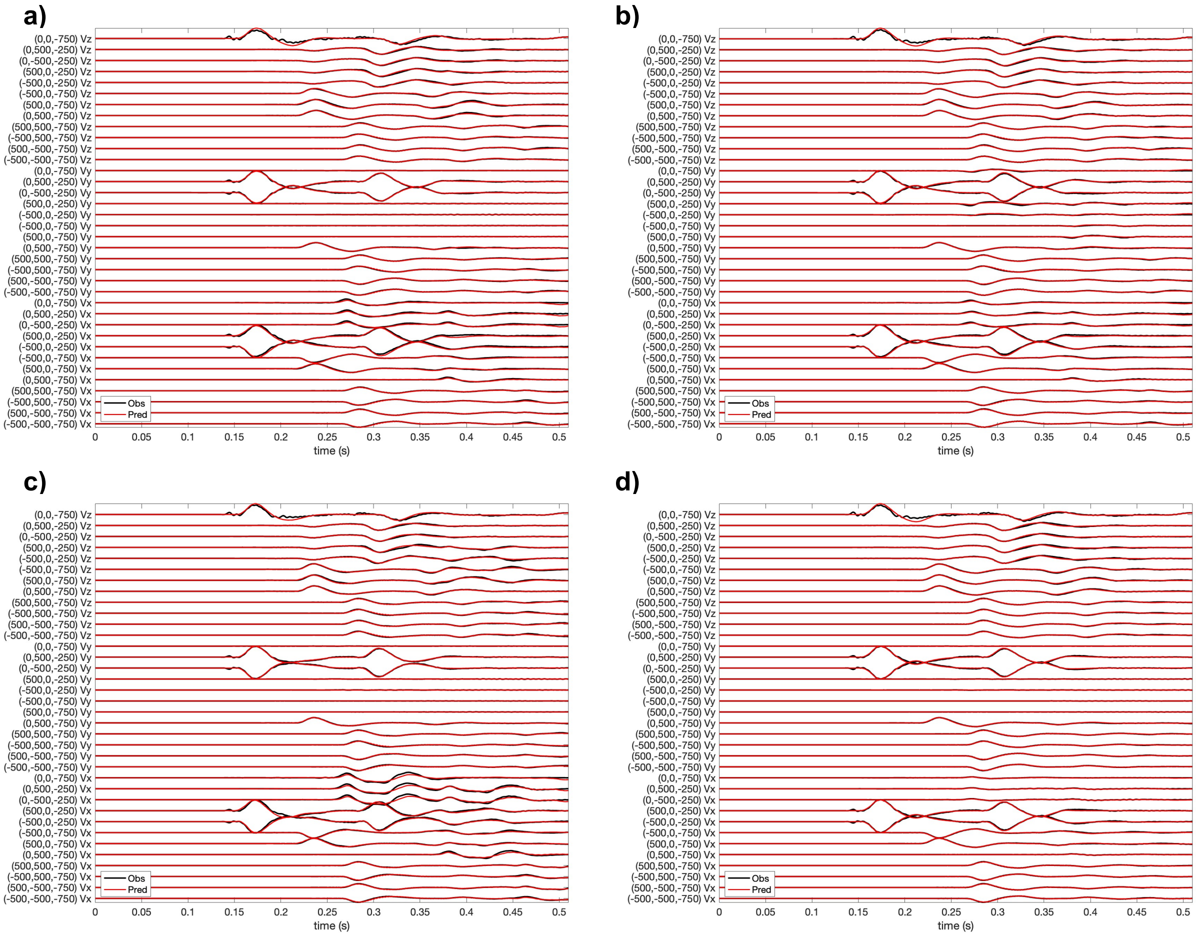

Figure 3.5: Observed (i.e., derived from CTH) black traces compared to predicted (red) based on the complete source (explosion plus force source terms) for select receiver locations labeled on y-axis for a) infinite cylinder, b) half cylinder, c) 11 m diameter air-filled sphere, and d) 11 m diameter basalt sphere cases.

the observed data are shown for multiple receiver locations in Figure 3.5a. Overall, the fit with this linear equivalent source is quite good, indicating that to first order, from the perspective of far-field seismic observations, the source looks like an explosion plus a force directed inline with the source to cylinder direction where the shock front most directly hits the cylinder walls.

3.2. Half-Infinite Cylinder

The half-infinite cylinder case ("halfTun" in figures) consists of a 3 m diameter air-filled cylinder with its center 12 m offset in the x-direction from the source point that runs "infinitely" in only the minus y direction with its termination at y = 1.5 m. This represents a well-stemmed explosion that is placed just off the terminus of a tunnel system. Similar to the infinite tunnel, we observe strong shear waves generated on Vx in the y and z directions and similar small differences on other channels (Figures 3.1-3.3; Appendix A) as was discussed for the infinite tunnel. One major difference, however, is the appearance of strong shear waves on Vy in the x and z directions (Figure 3.2a,b,e,f; A.7, A.8, A.11, A.12). Many of the waveforms show a transition if one looks along the y-dimension. Waveforms are very similar to the infinite tunnel waveforms for receivers near the minimum y range of receivers, whereas at the extreme positive y receiver locations, the half tunnel merges with the baseline waveforms (Figure 3.2f; A.12).

The strong Vy radiation pattern is indicative of a horizontal force source directed in the y-direction (Fy) in addition to explosion and Fx sources. Figure 3.4b shows the Fx and Fy STF portions and Figure 3.4a shows the explosion STF portion for this case, while Figure 3.5b shows how well the combination of these three sources fits the observations. The fits to Vy are not generally as good as to Vx or Vz, but this linear equivalent source does a reasonable job reproducing the observed data. The explosion STF has a peak amplitude intermediate between the baseline and infinite tunnel case with a ~9% reduction in peak moment compared to baseline.

3.3. 3 m Diameter Spheres

The two 3 m diameter sphere cases, one filled with air, the other with basalt, are visually virtually indistinguishable from the baseline waveforms. Zooming in one can see differences but these are much smaller than any other cases. In fact, the inverted STFs for both 3 m spheres are virtually identical to the baseline STF with the both peak moments within ~0.3% of the baseline. The air-filled sphere tends to produce somewhat larger differences from baseline than the basalt-filled sphere, but again differences are basically negligible on the far-field wavefield at these frequencies.

3.4. 11 m Diameter Spheres

The air-filled 11 m diameter sphere tends to have the largest deviations from the baseline waveforms of all cases, which is especially apparent for Vx on receivers in the y and z directions (Figure 3.1c-f; A.3-A.6). The 11 m diameter basalt sphere, on the other hand, generally has smaller perturbations from baseline than either the infinite or half tunnel cases. However, it shows the same spatial pattern in its perturbations as does the air-filled sphere, with the largest differences compared to baseline for Vx on receivers in the y and z directions with very little perturbation on Vy. Like the infinite cylinder case, this suggests an Fx plus an explosion for the linear source equivalent. Figure 3.4 shows the two STFs for both of the 11 m sphere cases. The explosion STF for the 11 m basalt sphere (Figure 3.4a) shows a fairly small reduction in peak moment with ~4% smaller moment than the tamped case. However, the 11 m diameter air-filled sphere demonstrates the largest reduction compared to baseline with a peak moment ~24% smaller than the tamped case. The Fx STF for the air-filled sphere tends to lie between that of the cylinders and basalt sphere, but with a much stronger pulse within the first ~0.1 s compared to the others, especially compared to the basalt sphere (Figure 3.4b). The combined explosion+Fx sources fit the data well for the air-filled sphere case (Figure 3.5c) and very well for the basalt sphere (Figure 3.5d).

3.5. Discussion

It is not overly surprising that 3 m diameter spheres, regardless of their composition, when outside the immediate location of the source, are nearly invisible to the far-field seismic wavefield at these modeled frequencies. Being ~3% of the minimum shear wavelength (assuming the filter cutoff frequency of 17 Hz is the highest frequency) and being observed multiple wavelengths from the source of the scatterer, the wavefield has had ample opportunity to "heal" with only small perturbation compared to the baseline waveforms (e.g., Hung et al., 2001), and this applies to small objects within the nonlinear portion of the wavefield like it does in the linear seismic regime, at least at this scale. However, the 11 m air-filled sphere, at ~10% of the minimum wavelength, does significantly affect the wavefield and estimated STF amplitudes with a reduction in estimated peak moment by ~24% compared to the tamped case. The composition of the sphere also has a significant impact with the same sized sphere filled with basalt only showing a fairly small reduction in estimated moment by ~4%.

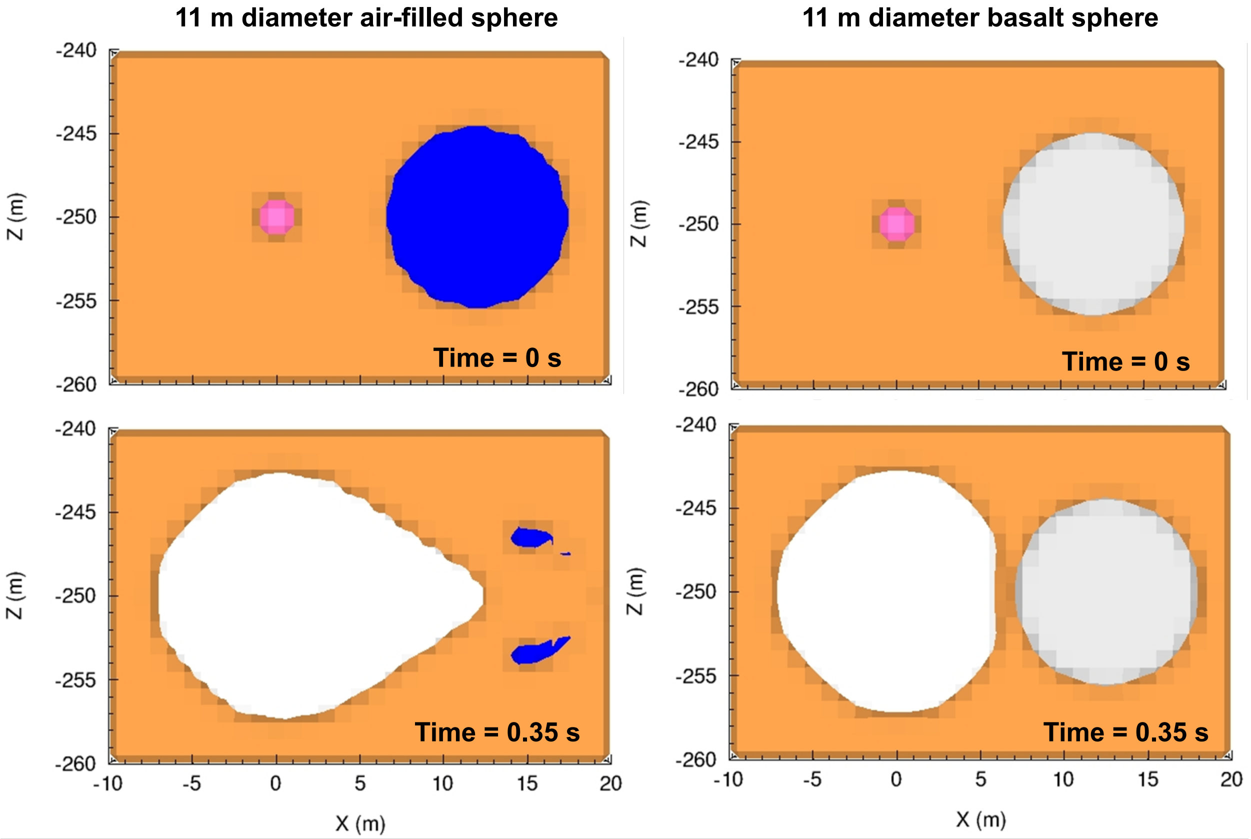

Figure 3.6: Nonlinear evolution of the near-source region of the 11 m diameter air-filled sphere (left) and basalt sphere (right) cases from its pre-detonation state (top) and at 0.35 s post-detonation (bottom). Blue: air, light gray: basalt, Peru color: host rock, pink: explosive charge, white: explosive byproducts.

The strong response of the 11 m air-filled sphere relative to the 11 m basalt sphere is likely due in large part to the air-filled cavity collapsing from the shock, whereas neither the cylinders nor any of the other spheres showed signs of collapse (Figure 3.6). Cavity collapse is clearly a nonlinear effect demonstrating that at least for some structures diffraction theory is insufficient to estimate the effects of small-scale structures on seismic signals. A stronger geologic material for the host rock or having the same size air-filled structure farther from the source point would be expected to reduce or eliminate the collapse portion of the signal and should be evaluated in future studies.

The tunnels have the same diameters as the 3 m spheres but present a broad surface, multiple wavelengths in length, in one dimension that the wavefield constantly interacts with, thus producing a clearly discernible impact on the seismic wavefield. This, in turn, reduces the moment estimates for the tunnel models by roughly 10% compared to baseline most likely due to scattering of initial P-wave energy into later portions of the wavefield.

These results demonstrate how even relatively small structures, if not fully accounted for in the models, can have a measurable impact on seismological quantities of interest. The presence of non-isotropic moment tensor components via the force sources does indicate that the scattered energy appears, from the far-field seismic perspective, to be due to other source types and is not simply "lost". However, given the complexity of the real Earth, filled with 3D variations, faults, fractures, and layers coupled with human-caused alterations to the natural geologic media, not all of which is known or can be used in simulations, this further points to the need for robust uncertainty quantification of seismic moment tensor solutions to account for Earth model uncertainty (e.g., Poppeliers and Preston, 2020; Poppeliers and Preston, 2022).

4. SUMMARY AND FUTURE DIRECTIONS

We built upon our prior work, which assumed 2D cylindrical symmetry, to include simulations using 3D nonlinear-to-linear computations. We used the nonlinear shock physics code CTH with embedded small-scale, near-source structures within an otherwise homogeneous half space to evaluate the effects of these 3D structures on the far-field seismic wavefield and resulting linear source equivalents. Cylinders, designed to represent tunnels near the source location, and spheres meant to represent perturbations to the surrounding medium of a size much less than a wavelength, were evaluated.

We found that, just as may be expected from linear seismic diffraction theory, the 3 m diameters spheres within the shock regime also were nearly invisible within the far-field seismic wavefield containing frequencies < ~17 Hz, with only minor perturbations observed relative to the baseline wavefield and seismic moment with no 3D structures present. Likewise, the 11 m basalt sphere caused relatively small perturbations to the baseline wavefield with only ~4% reduction in estimated moment relative to the tamped case. The 11 m diameter air-filled sphere, on the other hand, demonstrated the largest deviations from the baseline waveforms and moment estimates derived from them of any of the cases with a reduction of ~24% in estimated moment relative to the baseline peak moment, most likely due in large part to the collapse of the cavity post-detonation. The air-filled infinite and semi-infinite cylinders, which have the same diameters as the 3 m spheres, also do have a clear impact on the observed seismic waveforms and on the estimated source time functions. Strong S-waves are generated by the cylinders and 11 m spheres that appear from the linear seismic perspective to be generated from horizontal body force sources. The shear wave radiation patterns are consistent with a force source directed parallel to the vector pointing from the source point to the center of both cylinders and spheres. In addition, the half-infinite cylinder appeared to generate S-waves consistent with a body force directed perpendicular to the terminal face of the tunnel. The explosion STFs derived for the tunnels had reductions of 9% and 13% in peak moment relative to baseline for the half-infinite and infinite cylinders, respectively. Overall, these results indicate that small-scale structures near the source can strongly impact the far-field seismic wavefield and quantities derived from them (e.g., seismic moment), especially if significant nonlinear deformation of those structures, such as cavity collapse, occurs due to the explosion.

Since seismic moment is a primary means of estimating the yield of explosions, these results underscore the importance of accurate Earth models, including any man-made structures, in seismic moment estimates. As our results demonstrate, how much these structures affect seismic moment depends on the dimensions of the structure relative to the wavelengths present (frequency content) in the observed seismic wavefield and on the nonlinear deformation of those structures. Provided that the uncertainty in the Earth model is often one of the largest sources of uncertainty in moment tensor inversion, in the absence of well characterized and accurate Earth models, it is important to be cognizant of the effects that even relatively small structures, whether natural or man-made, near the source can have on moment estimates. We plan on continuing our investigations of how heterogeneities in the near-source region impact moment estimates with application to experimental data supported by simulations.

REFERENCES

1. Aki, K., and P.G. Richards (2002). *Quantitative Seismology*, Second Edition, University Science Books, Sausalito, CA.
2. Aldridge, D.F. (2000). *Radiation of elastic waves from point sources in a uniform wholespace*, SAND2000-1767, Sandia National Laboratories, Albuquerque, NM.
3. Aldridge, D.F, and M.M. Haney (2008). *Numerical dispersion for the conventional-staggered-grid finite-difference elastic wave propagation algorithm*, SAND2008-4991, Sandia National Laboratories, Albuquerque, NM.
4. Eliassi, M., and L.A. Preston (2022). *Effects of model uncertainties in underground chemical explosions on far-field results*, SAND2022-1360, Sandia National Laboratories, Albuquerque, NM.
5. Harding, J.L., L.A. Preston, and M. Eliassi (in review). The influence of physical and algorithmic factors on simulated far-field waveforms and source time functions of underground explosions using unsupervised machine learning, submitted to *Geophy. J. Int.*
6. Hestenes, M.R., and E. Stiefel (1952). Methods of conjugate gradients for solving linear systems, *J. Res. N.B.S.*, 49, 409-436.
7. Hung, S.-H., F.A. Dahlen, and G. Nolet (2001). Wavefront healing: a banana-doughnut perspective, *Geophys. J. Int.*, 146, 289-312.
8. Lay, T., and T.C. Wallace (1995). *Modern Global Seismology*, Academic Press, San Diego, CA.
9. Poppeliers, C., and L. Preston (2020). The effects of earth model uncertainty on the inversion of seismic data for seismic source functions, *Geophys. J. Int.*, 224, 100-120, doi:10.1093/gji/ggaa408.
10. Poppeliers, C., and L. Preston (2022). An efficient method to propagate model uncertainty when inverting seismic data for time domain seismic moment tensors, *Geophy. J. Int.*, doi:10.1093/gji/ggac227.
11. Preston, L. (2017). *Nonlinear to linear elastic code coupling in 2-D axisymmetric media*, SAND2017-8848, Sandia National Laboratories, Albuquerque, NM.
12. Preston, L., M. Eliassi, and C. Poppeliers (2021a). *Programmatic advantages of linear equivalent seismic models*, SAND2021-10201, Sandia National Laboratories, Albuquerque, NM.
13. Preston, L., C. Poppeliers, and M. Eliassi (2021b). *FY21 seismic source modeling software enhancements*, SAND2021-10785, Sandia National Laboratories, Albuquerque, NM.
14. Schmitt, G., D.A. Crawford, E.N. Harstad, D.M. Hensinger, and K.P. Ruggirello, (2017). *CTH User's Manual and Input Instructions, Version 12.0, CTH Development Projects*, Sandia National Laboratories, Albuquerque, NM. (OUO).

A. SEISMOGRAM COMPARISONS BY CASE

This appendix provides figures of all three components of the far-field seismic velocity field on 6 sets of lines of receivers for all the cases. These are meant as a comparison of specific waveform features from case to case.

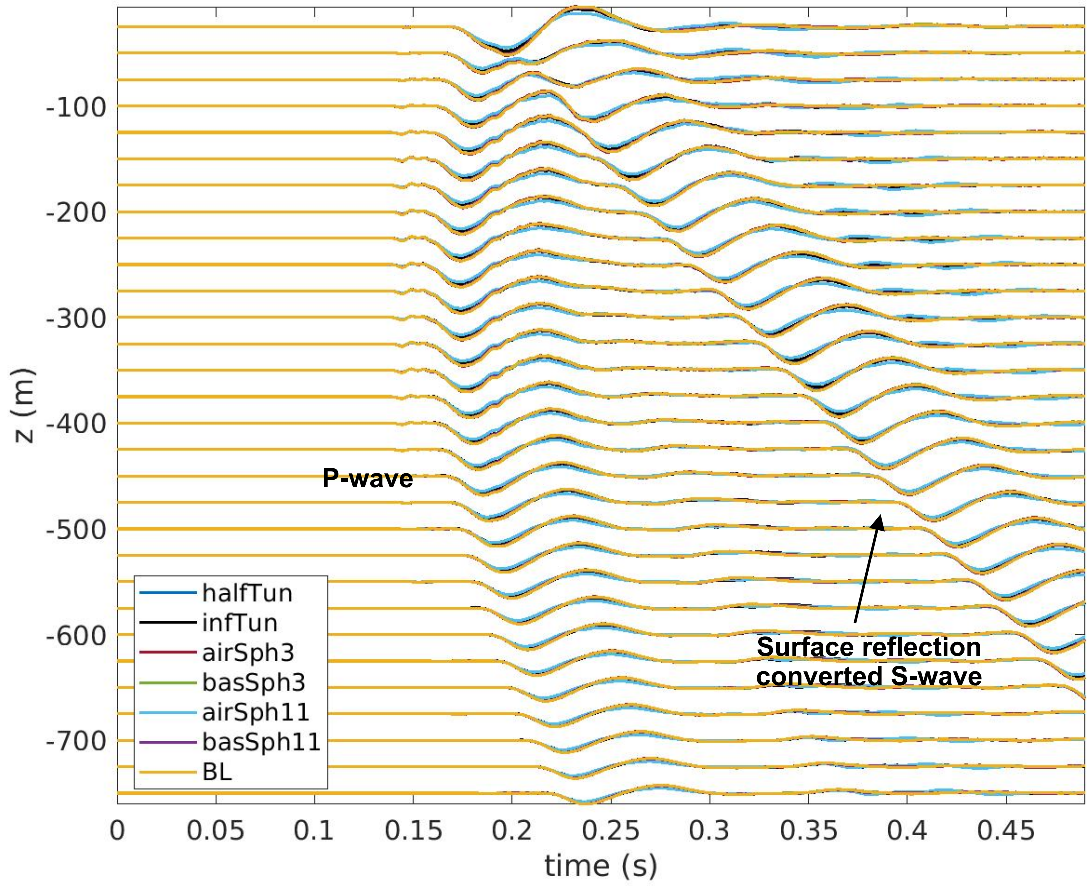

Figure A.1: Comparison of seismic waveforms among different cases for Vx: infinite tunnel, half-tunnel, 3 m diameter air-filled sphere, 3 m basalt sphere, 11 m air-filled sphere, 11 m basalt sphere, and baseline (BL) at x=500 and y=0 m. Prominent seismic arrivals are labeled.

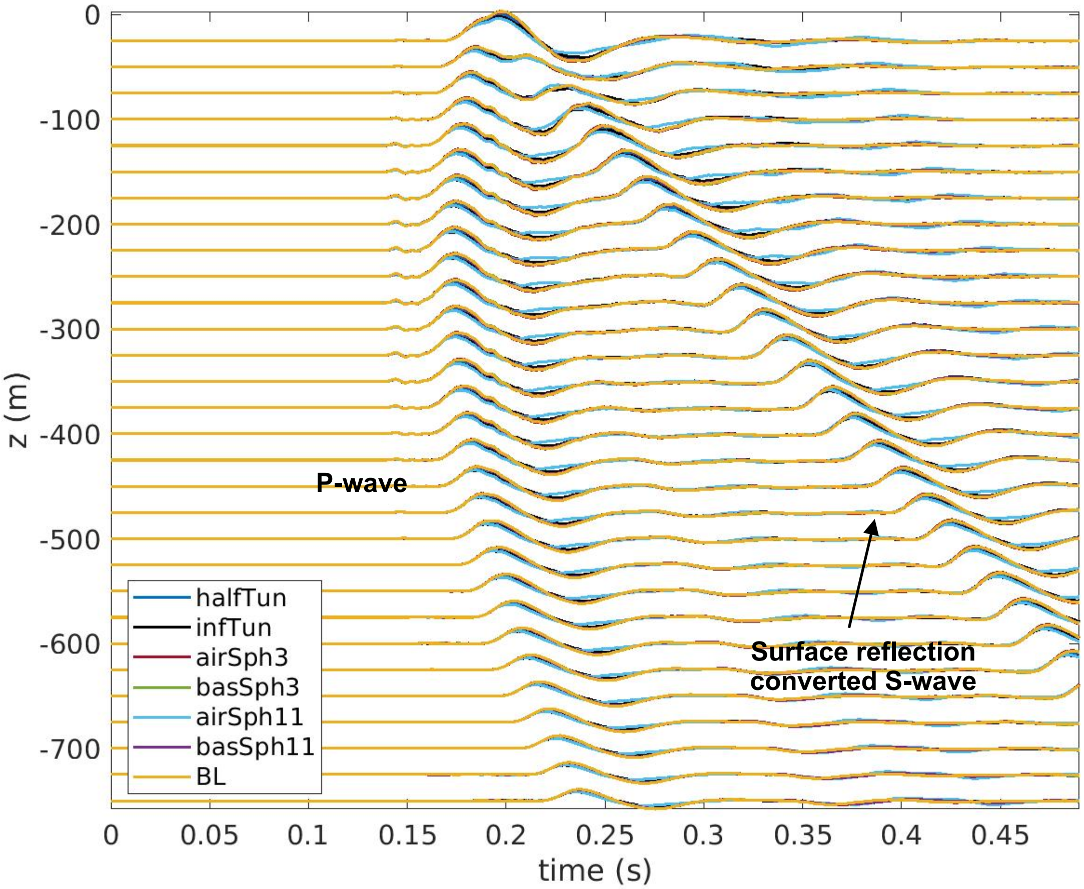

Figure A.2: Comparison of seismic waveforms among different cases for Vx: infinite tunnel, half-tunnel, 3 m diameter air-filled sphere, 3 m basalt sphere, 11 m air-filled sphere, 11 m basalt sphere, and baseline (BL) at x=-500 and y=0 m. Prominent seismic arrivals are labeled.

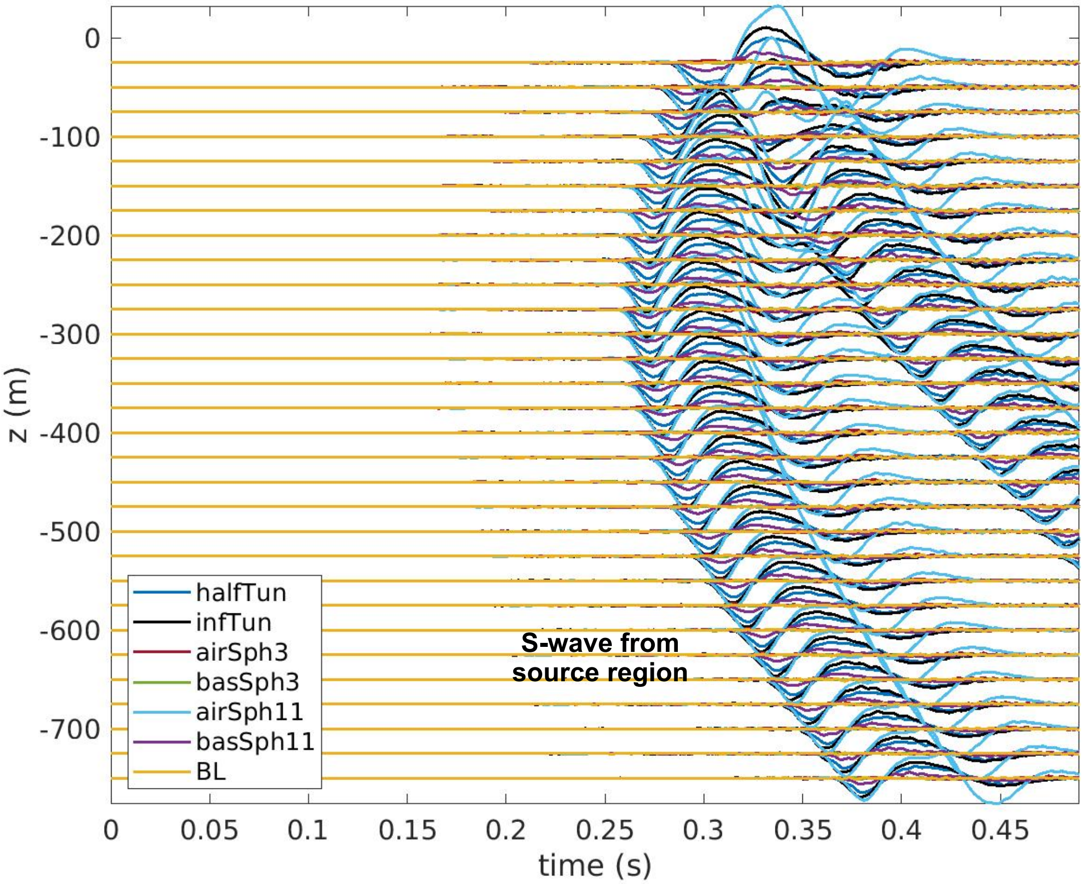

Figure A.3: Comparison of seismic waveforms among different cases for Vx: infinite tunnel, half-tunnel, 3 m diameter air-filled sphere, 3 m basalt sphere, 11 m air-filled sphere, 11 m basalt sphere, and baseline (BL) at y=500 and x=0 m. Prominent seismic arrivals are labeled.

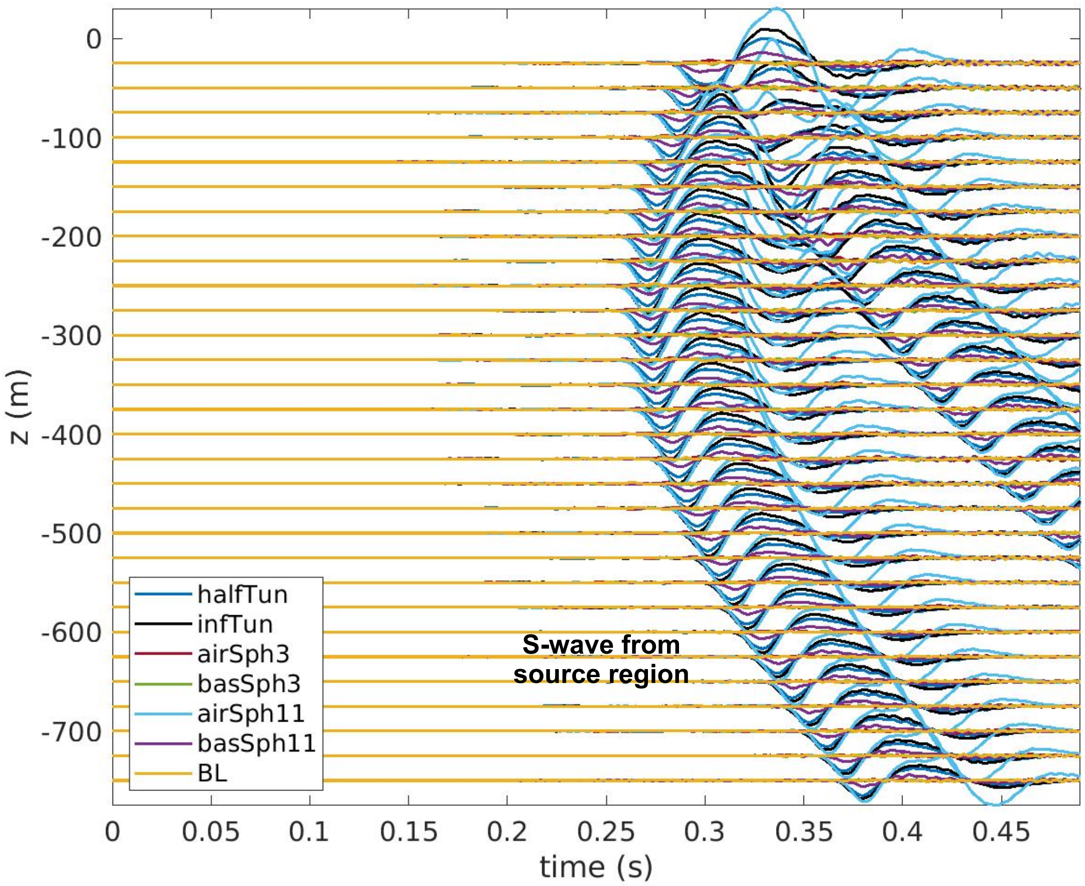

Figure A.4: Comparison of seismic waveforms among different cases for Vx: infinite tunnel, half-tunnel, 3 m diameter air-filled sphere, 3 m basalt sphere, 11 m air-filled sphere, 11 m basalt sphere, and baseline (BL) at y=-500 and x=0 m. Prominent seismic arrivals are labeled.

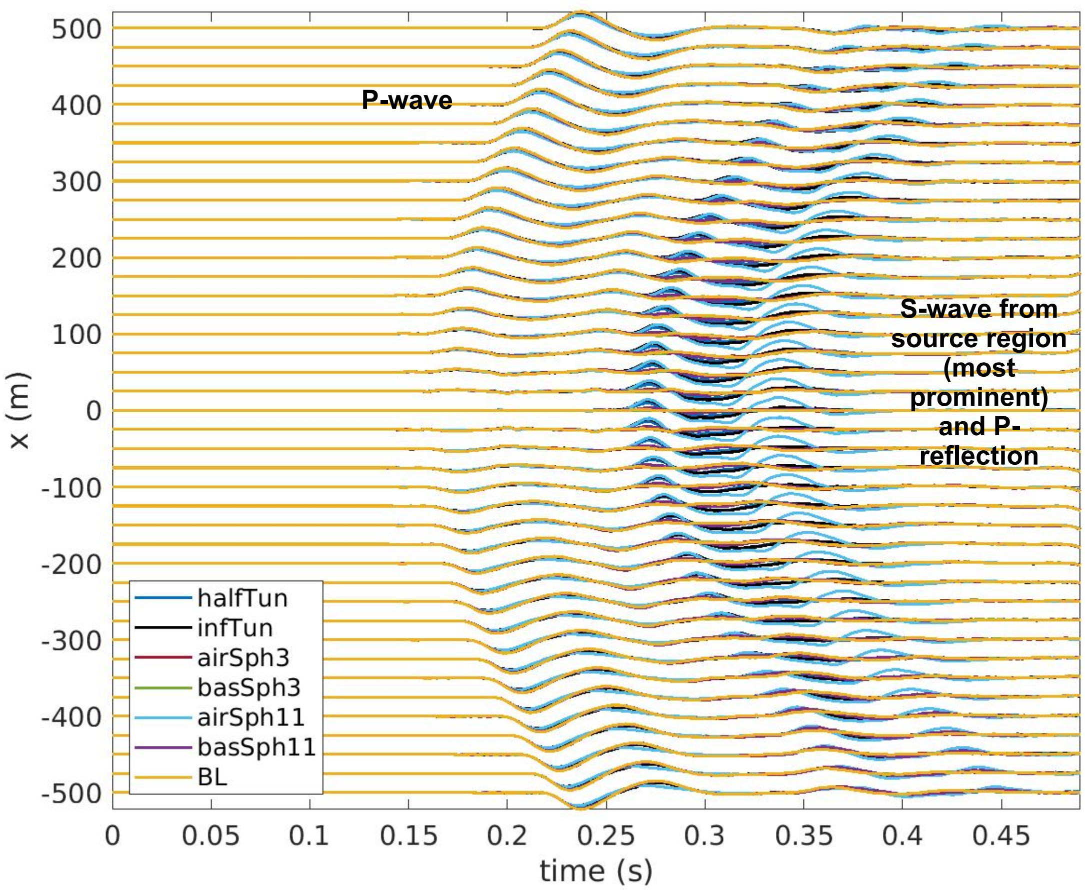

Figure A.5: Comparison of seismic waveforms among different cases for Vx: infinite tunnel, half-tunnel, 3 m diameter air-filled sphere, 3 m basalt sphere, 11 m air-filled sphere, 11 m basalt sphere, and baseline (BL) at y=0 and z=-750 m. Prominent seismic arrivals are labeled.

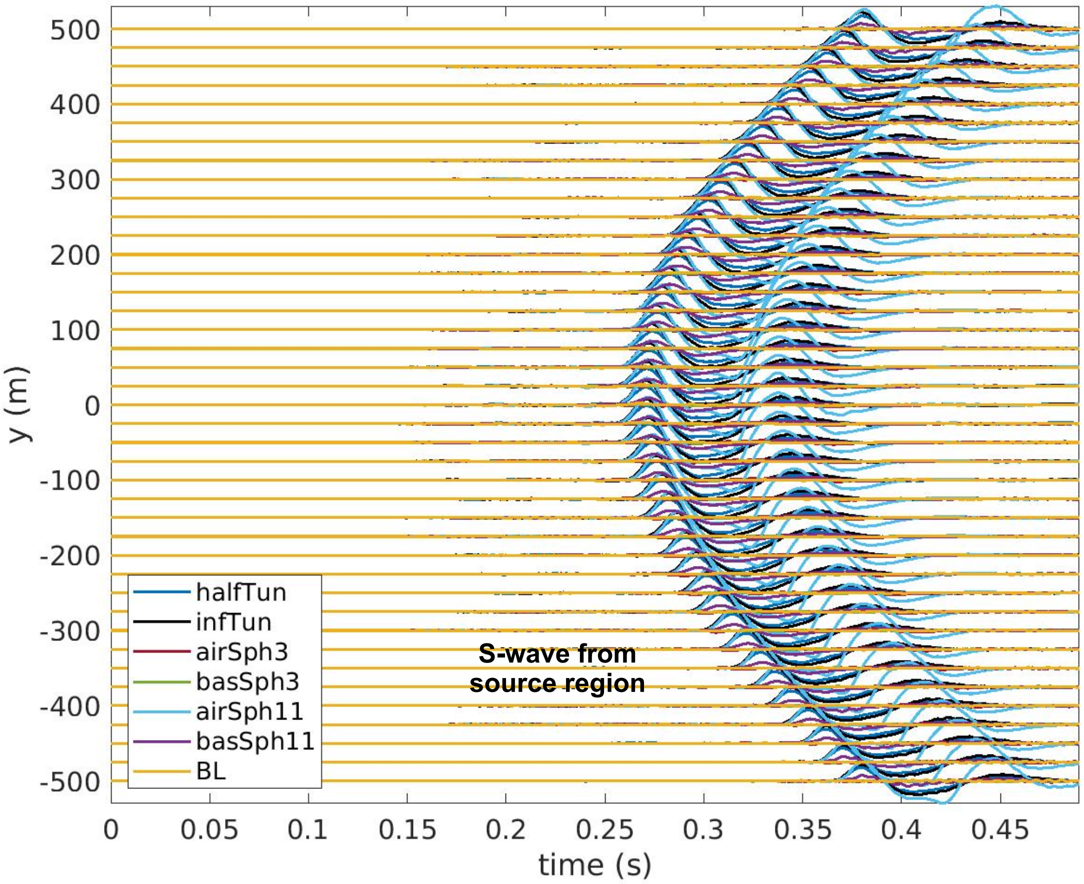

Figure A.6: Comparison of seismic waveforms among different cases for Vx: infinite tunnel, half-tunnel, 3 m diameter air-filled sphere, 3 m basalt sphere, 11 m air-filled sphere, 11 m basalt sphere, and baseline (BL) at x=0 and z=-750 m. Prominent seismic arrivals are labeled.

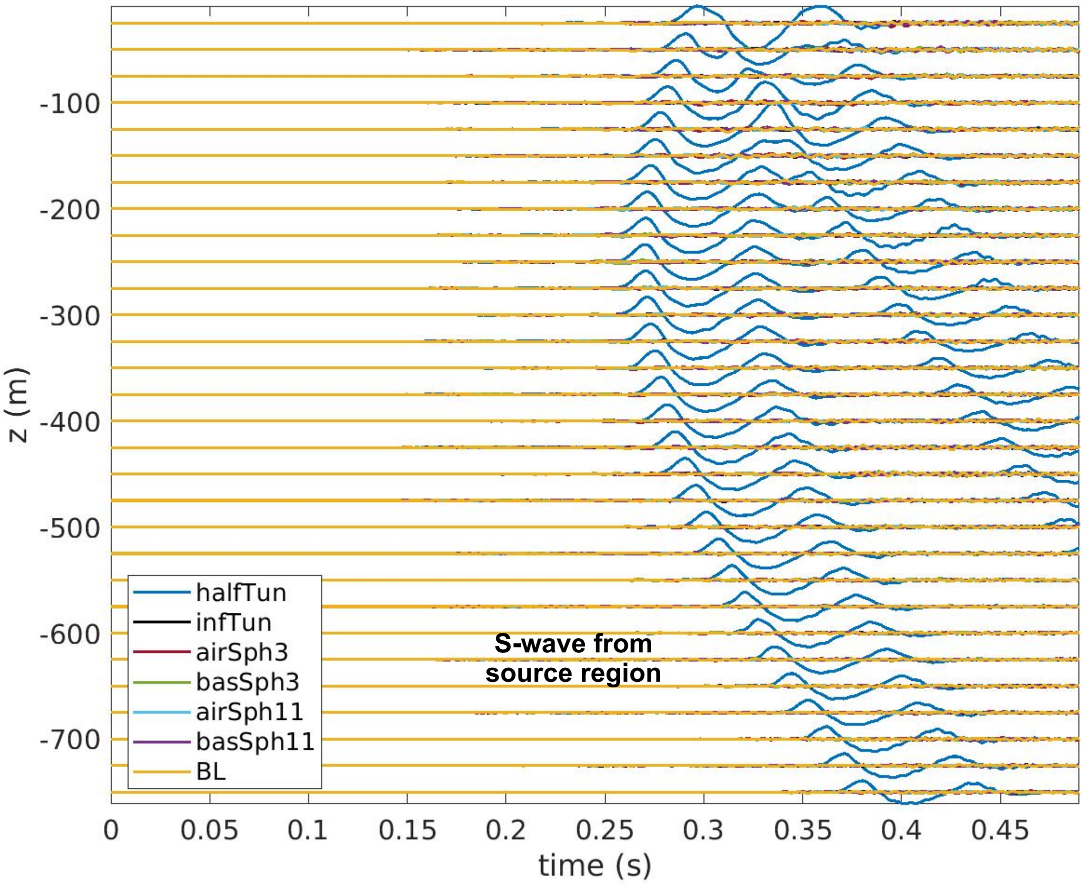

Figure A.7: Comparison of seismic waveforms among different cases for Vy: infinite tunnel, half-tunnel, 3 m diameter air-filled sphere, 3 m basalt sphere, 11 m air-filled sphere, 11 m basalt sphere, and baseline (BL) at x=500 and y=0 m. Prominent seismic arrivals are labeled.

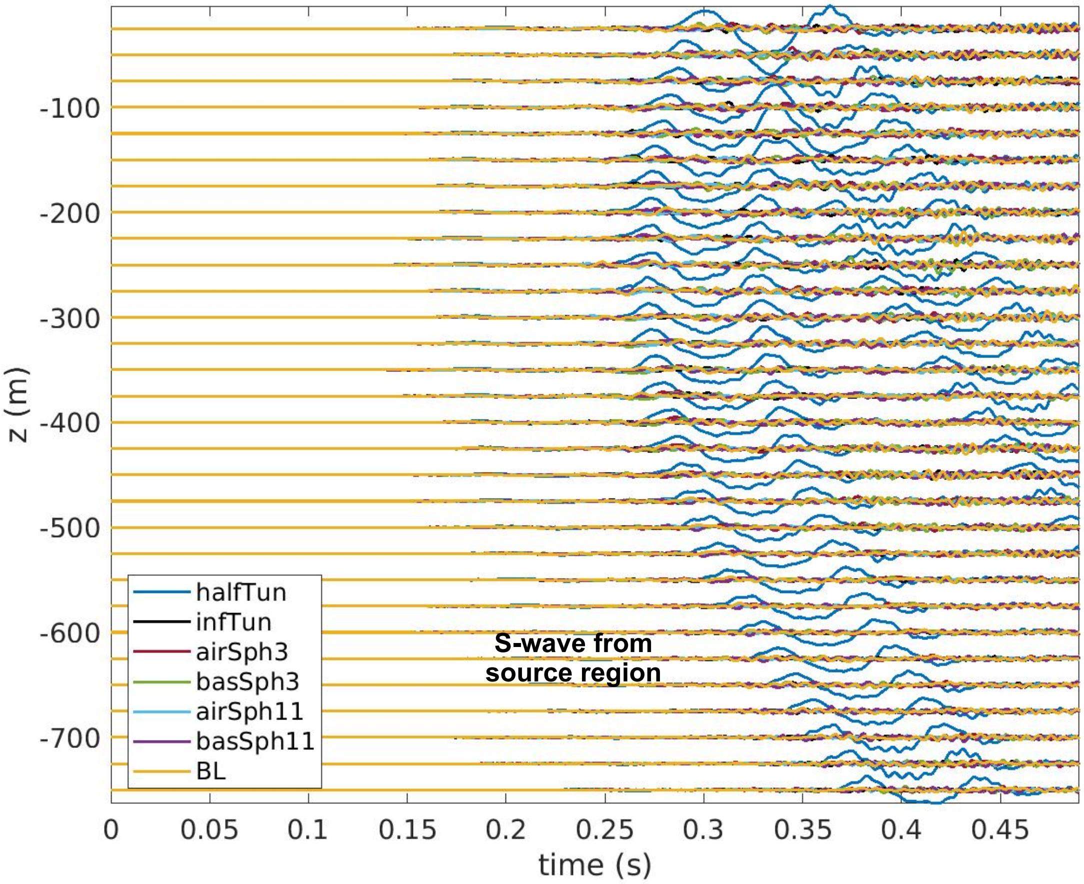

Figure A.8: Comparison of seismic waveforms among different cases for Vy: infinite tunnel, half-tunnel, 3 m diameter air-filled sphere, 3 m basalt sphere, 11 m air-filled sphere, 11 m basalt sphere, and baseline (BL) at x=-500 and y=0 m. Prominent seismic arrivals are labeled.

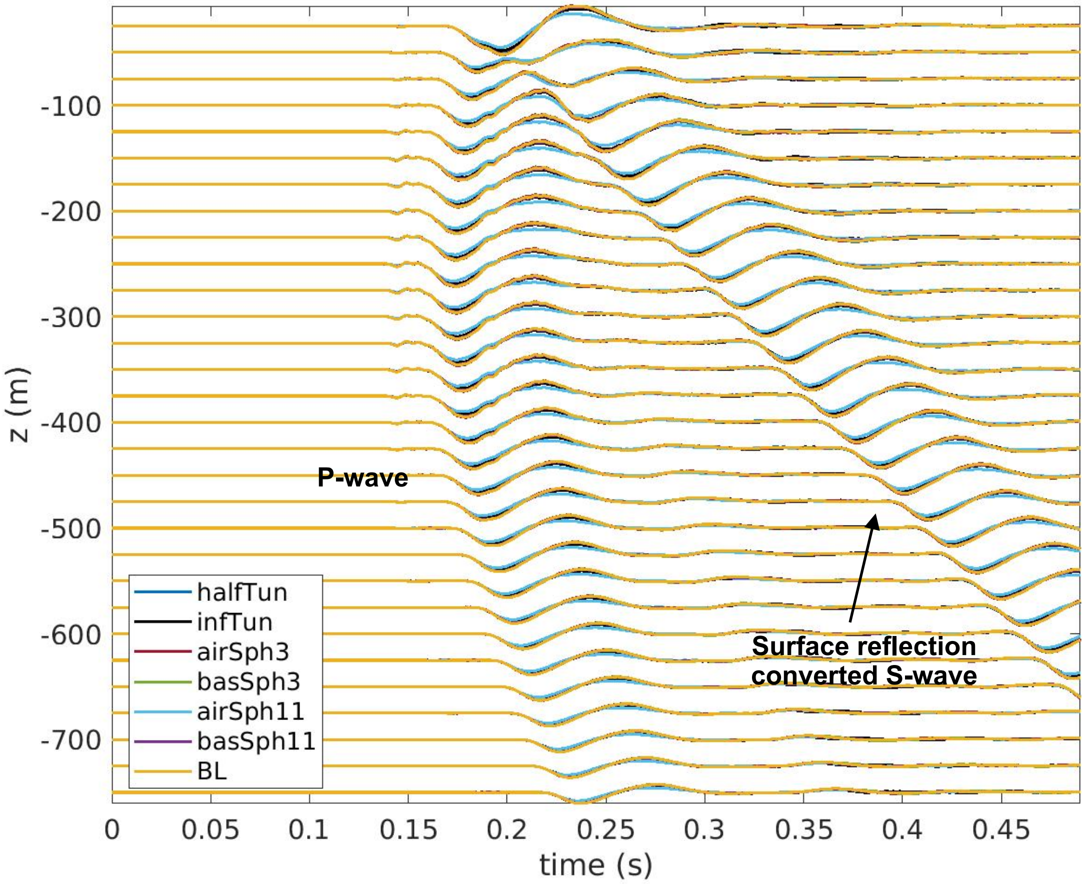

Figure A.9: Comparison of seismic waveforms among different cases for Vy: infinite tunnel, half-tunnel, 3 m diameter air-filled sphere, 3 m basalt sphere, 11 m air-filled sphere, 11 m basalt sphere, and baseline (BL) at x=0 and y=500 m. Prominent seismic arrivals are labeled.

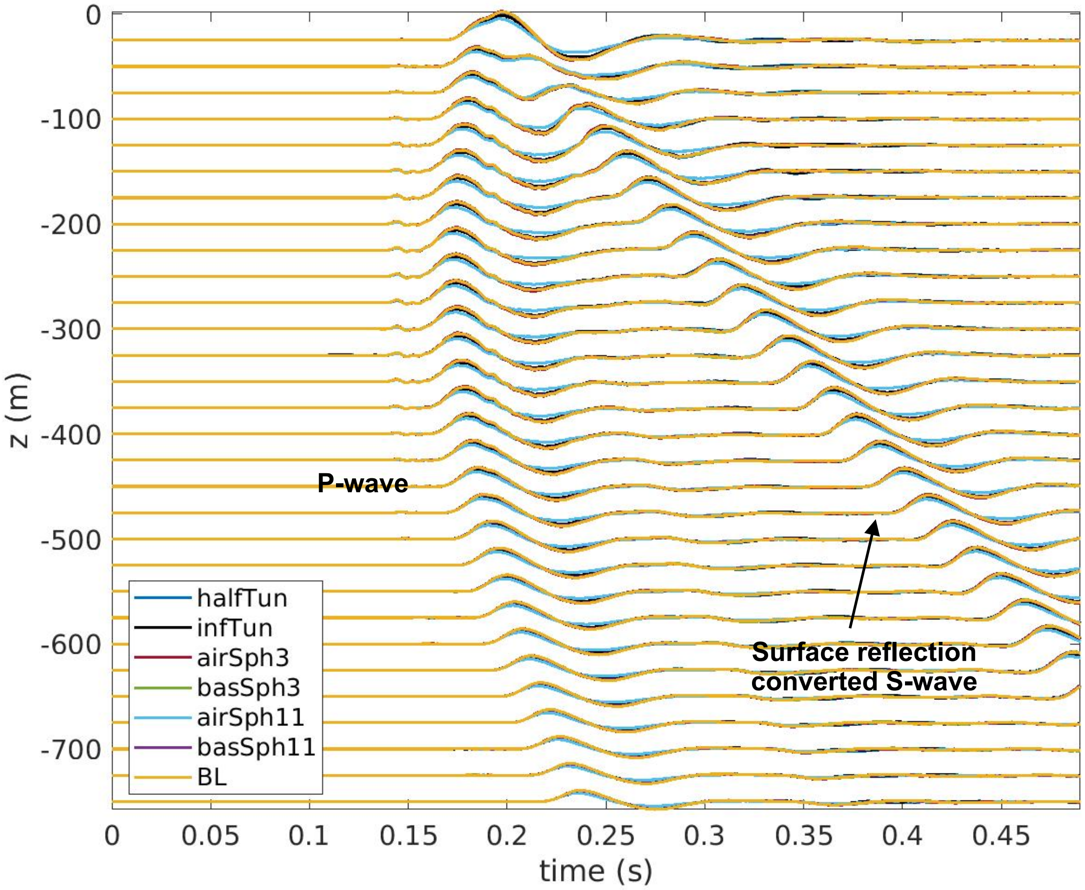

Figure A.10: Comparison of seismic waveforms among different cases for Vy: infinite tunnel, half-tunnel, 3 m diameter air-filled sphere, 3 m basalt sphere, 11 m air-filled sphere, 11 m basalt sphere, and baseline (BL) at x=0 and y=-500 m. Prominent seismic arrivals are labeled.

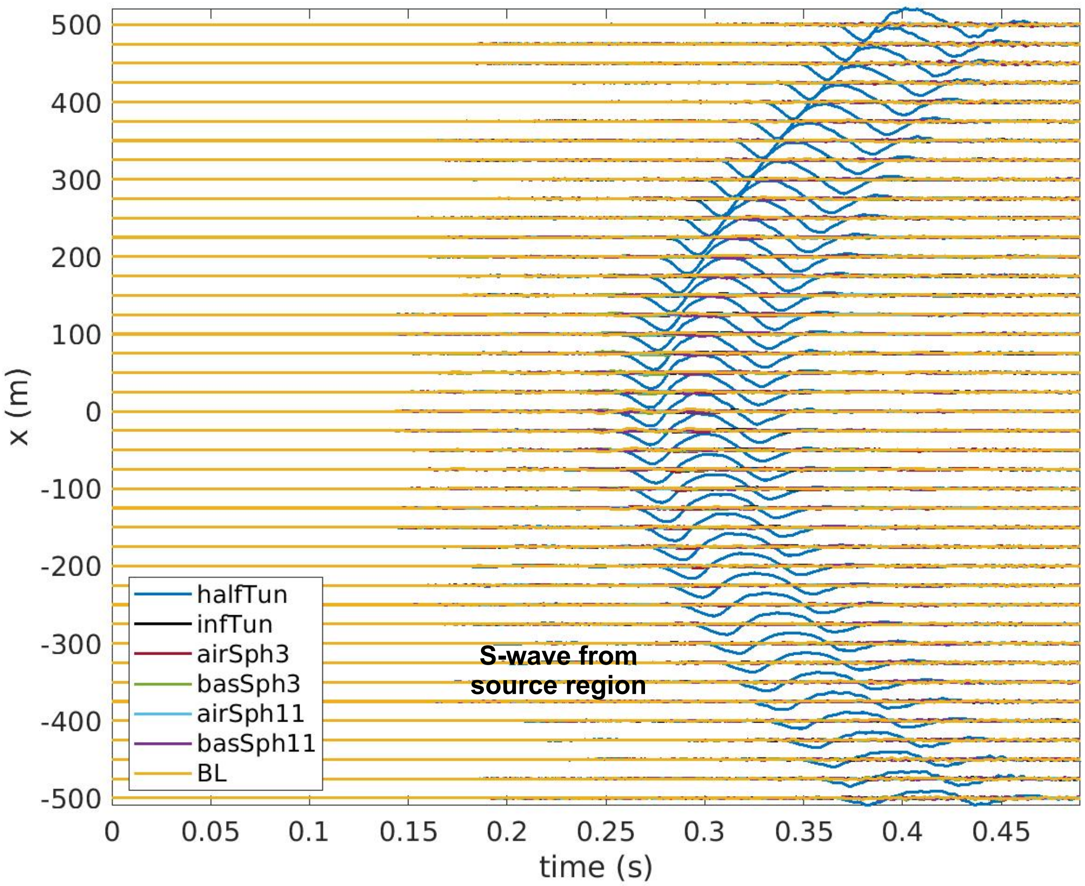

Figure A.11: Comparison of seismic waveforms among different cases for Vy: infinite tunnel, half-tunnel, 3 m diameter air-filled sphere, 3 m basalt sphere, 11 m air-filled sphere, 11 m basalt sphere, and baseline (BL) at y=0 and z=-750 m. Prominent seismic arrivals are labeled.

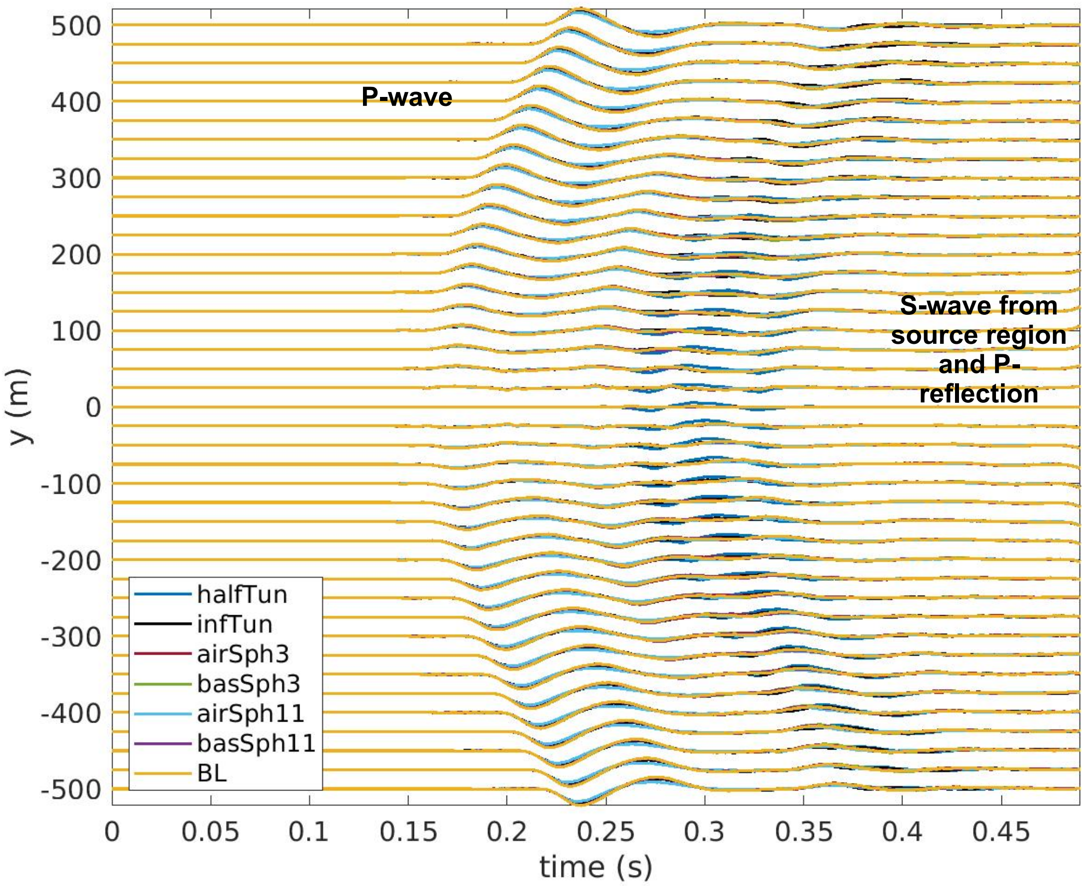

Figure A.12: Comparison of seismic waveforms among different cases for Vy: infinite tunnel, half-tunnel, 3 m diameter air-filled sphere, 3 m basalt sphere, 11 m air-filled sphere, 11 m basalt sphere, and baseline (BL) at x=0 and z=-750 m. Prominent seismic arrivals are labeled.

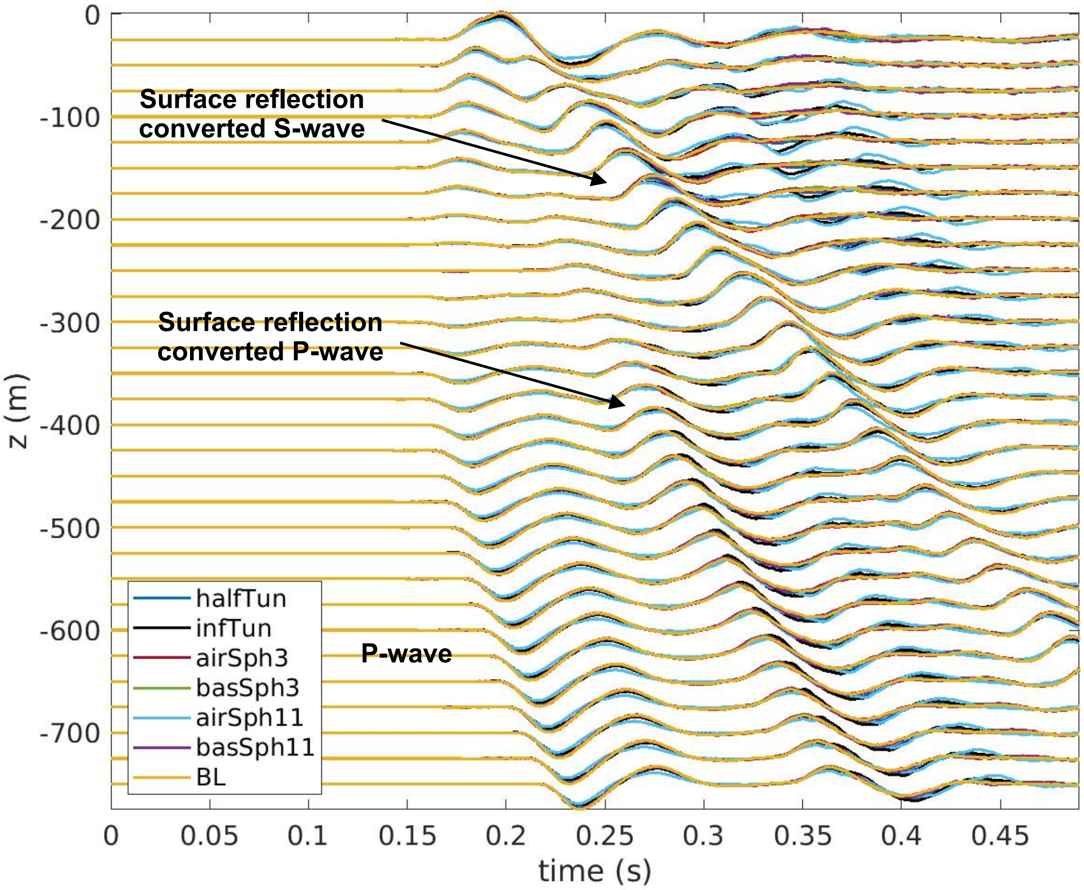

Figure A.13: Comparison of seismic waveforms among different cases for Vz: infinite tunnel, half-tunnel, 3 m diameter air-filled sphere, 3 m basalt sphere, 11 m air-filled sphere, 11 m basalt sphere, and baseline (BL) at x=500 and y=0 m. Prominent seismic arrivals are labeled.

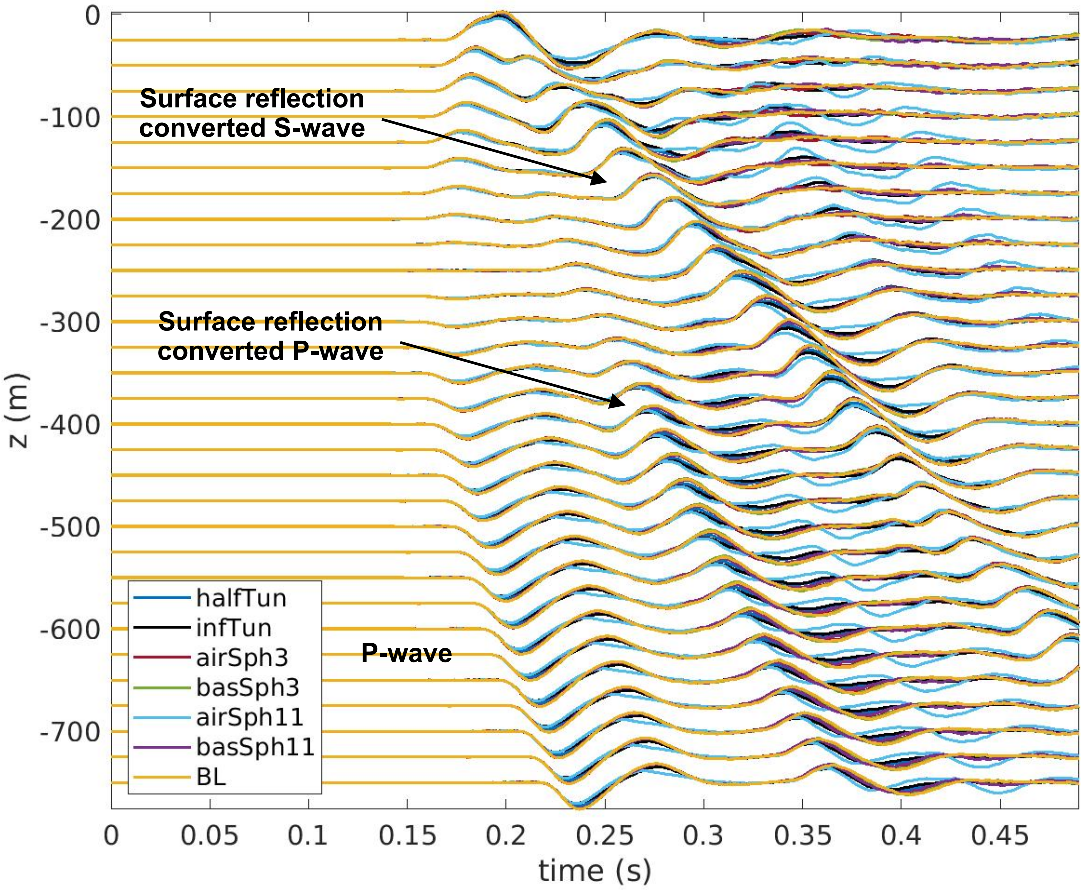

Figure A.14: Comparison of seismic waveforms among different cases for Vz: infinite tunnel, half-tunnel, 3 m diameter air-filled sphere, 3 m basalt sphere, 11 m air-filled sphere, 11 m basalt sphere, and baseline (BL) at x=-500 and y=0 m. Prominent seismic arrivals are labeled.

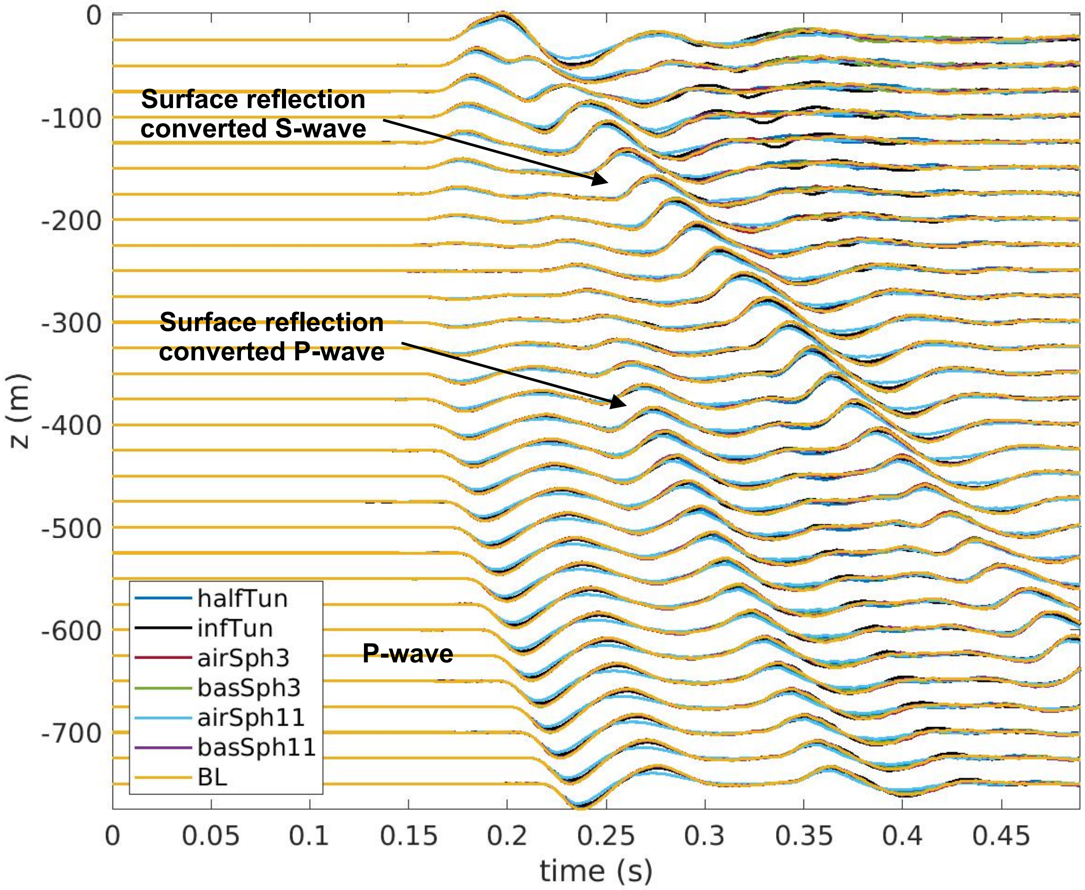

Figure A.15: Comparison of seismic waveforms among different cases for Vz: infinite tunnel, half-tunnel, 3 m diameter air-filled sphere, 3 m basalt sphere, 11 m air-filled sphere, 11 m basalt sphere, and baseline (BL) at x=0 and y=500 m. Prominent seismic arrivals are labeled.

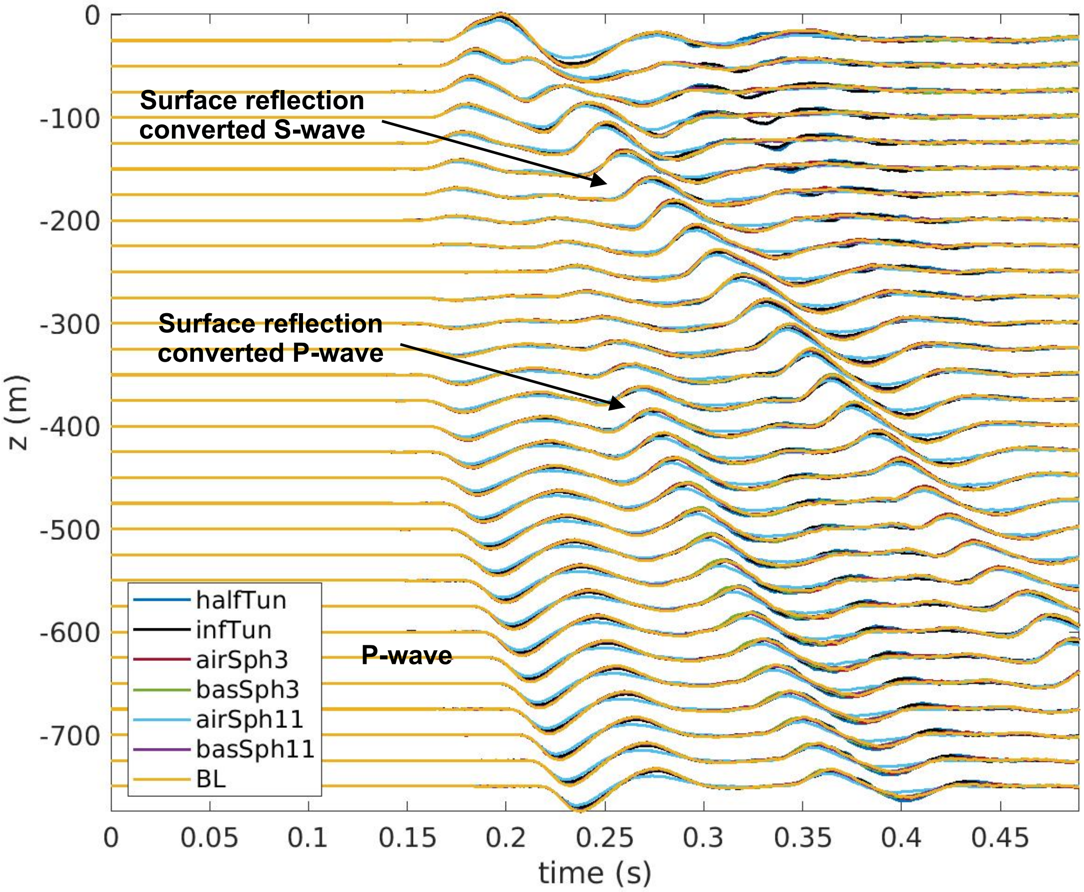

Figure A.16: Comparison of seismic waveforms among different cases for Vz: infinite tunnel, half-tunnel, 3 m diameter air-filled sphere, 3 m basalt sphere, 11 m air-filled sphere, 11 m basalt sphere, and baseline (BL) at x=0 and y=-500 m. Prominent seismic arrivals are labeled.

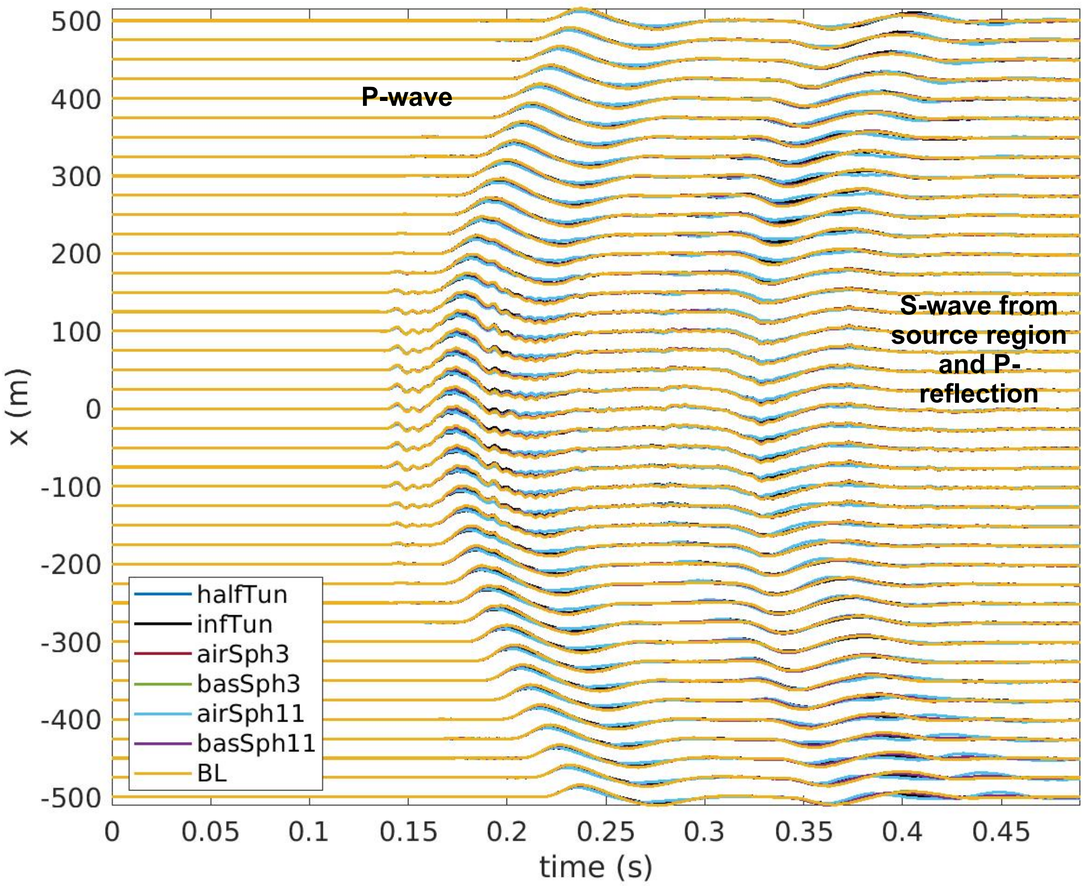

Figure A.17: Comparison of seismic waveforms among different cases for Vz: infinite tunnel, half-tunnel, 3 m diameter air-filled sphere, 3 m basalt sphere, 11 m air-filled sphere, 11 m basalt sphere, and baseline (BL) at y=0 and z=-750 m. Prominent seismic arrivals are labeled.

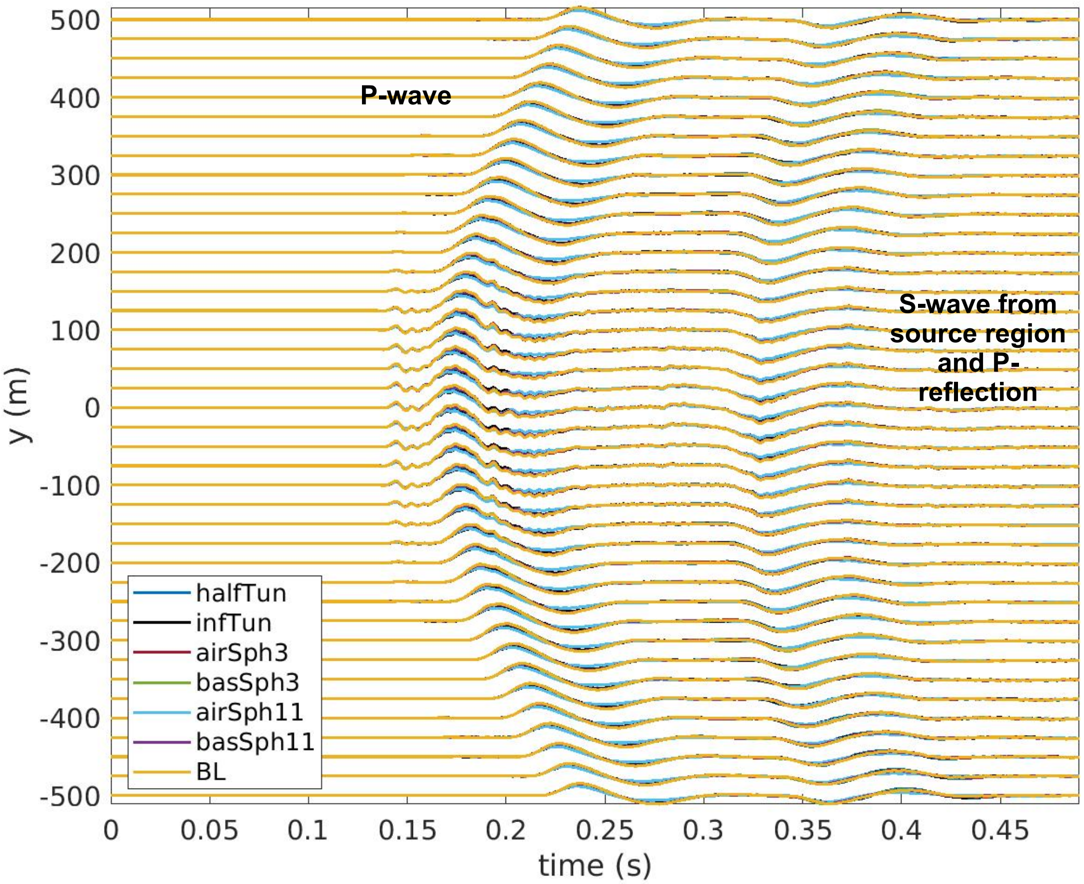

Figure A.18: Comparison of seismic waveforms among different cases for Vz: infinite tunnel, half-tunnel, 3 m diameter air-filled sphere, 3 m basalt sphere, 11 m air-filled sphere, 11 m basalt sphere, and baseline (BL) at x=0 and z=-750 m. Prominent seismic arrivals are labeled.

DISTRIBUTION

Email—Internal

Name	Org.	Sandia Email Address
Lauren Wheeler	8913	lwheele@sandia.gov
Technical Library	1911	sanddocs@sandia.gov

This page left blank